Journal of Computational Physics 229 (2010) 1327–1352

Contents lists available at ScienceDirect

Journal of Computational Physics

journal homepage: www.elsevier.com/locate/jcp

Reduced-order models for parameter dependent geometries based on shape sensitivity analysis

A. Hay [a,*], J. Borggaard [a], I. Akhtar [a], D. Pelletier [b]

[a] Interdisciplinary Center for Applied Mathematics, Virginia Tech, Blacksburg, VA 24060, USA
[b] Département de Génie Mécanique, Ecole Polytechnique de Montréal, Montréal, QC, Canada H3C3A7

ARTICLE INFO

Article history:
Received 11 March 2009
Received in revised form 3 August 2009
Accepted 19 October 2009
Available online 25 October 2009

Keywords:
Proper orthogonal decomposition
Reduced-order models
Sensitivity analysis
Shape parameters
Burgers' equation
Navier–Stokes equations

ABSTRACT

The proper orthogonal decomposition (POD) is widely used to derive low-dimensional models of large and complex systems. One of the main drawback of this method, however, is that it is based on reference data. When they are obtained for one single set of parameter values, the resulting model can reproduce the reference dynamics very accurately but generally lack of robustness away from the reference state. It is therefore crucial to enlarge the validity range of these models beyond the parameter values for which they were derived. This paper presents two strategies based on shape sensitivity analysis to partially address this limitation of the POD for parameters that define the geometry of the problem at hand (design or shape parameters.) We first detail the methodology to compute both the POD modes and their Lagrangian sensitivities with respect to shape parameters. From them, we derive improved reduced-order bases to approximate a class of solutions over a range of parameter values. Secondly, we demonstrate the efficiency and limitations of these approaches on two typical flow problems: (1) the one-dimensional Burgers' equation; (2) the two-dimensional flows past a square cylinder over a range of incidence angles.

1. Introduction

The proper orthogonal decomposition (POD) [1] has emerged as a powerful tool in fluid mechanics. Given a set of flow data, it extracts the most energetic global functions (modes) that can be used to characterize and analyze flows. Given the optimality of the POD modes in terms of energy representation, they are also good candidates to build low-dimensional models of the system dynamics using the Galerkin method (see e.g. [2–4] for more details on the POD). Flow modeling by POD-Galerkin systems has been the most popular approach in the literature (see e.g. [5–9]) though there is a number of other ways to generate global functions.

The accuracy of reduced-order models crucially depends on how good a reduced basis is to represent the targeted set of solutions. One of the issues that arises is to what extent bases obtained by decomposing flow data at one given set of parameter values (henceforth the reference or baseline state) can account for solutions over a wide range of parameter values. Indeed, the bases obtained by empirical selection methods are shown to be optimal (in a given sense) for the particular set of flow snapshots but are generally not well-suited to represent any solution of the PDE at hand (unlike polynomial or spectral bases used in finite-element for example). Thus, regardless of the truncation taken in the full-basis, the reduced basis ob-

---

* Corresponding author. Address: Industrial Materials Institute, National Research Council Canada, 75 de Mortagne, Boucherville, QC, Canada J4B6Y4. Tel.: +1 450 641 5422; fax: +1 450 641 5106.

E-mail addresses: alexander.hay@imi.cnrc-nrc.gc.ca (A. Hay), jborggaard@vt.edu (J. Borggaard), akthar@vt.edu (I. Akhtar), dominique.pelletier@polymtl.ca (D. Pelletier).

0021-9991/$ - see front matter © 2009 Elsevier Inc. All rights reserved.
doi:10.1016/j.jcp.2009.10.033

tained may not be able to accurately represent a range of solutions in the parameter space leading to inaccurate ROM. This drawback was reported in the literature for laminar flows over obstacles considering a range of Reynolds numbers [5].

In our previous studies [10,11], we have used sensitivity analysis in the basis selection process to enlarge the set of solutions that can be accurately represented in the parameter space, which in turn allows for more robust ROM. The proposed approaches all rely on the sensitivities of the POD modes (their derivatives with respect to parameters). They are derived by differentiating the eigenvalue problem for the POD modes. This yields a set of equations for the eigenvalue and eigenvector sensitivities that require flow sensitivity data. The latter have been obtained by the continuous sensitivity equation method (SEM) [12–14]. Using the POD mode sensitivities, we have examined two different approaches to derive bases that are adequate for a range of parameter values. The first one extrapolates the POD modes in the parameter space to the corresponding state to be modeled. It relies on the assumption that the eigenfunctions have a linear dependency on the parameters which can only be validated locally. The second one expands the reduced basis by adding the sensitivity of the original modes. The underlying idea behind this approach is that the POD mode sensitivities span a different subspace than the one generated by the POD eigenfunctions. Furthermore, this subspace is deemed appropriate to represent changes in solutions with parameter variations. In this previous work, the two-dimensional flow past a cylinder was considered since it has been widely used in the literature for assessing the accuracy of ROM [5,9,8,6,15]. Furthermore, the fluid viscosity was used as a parameter in the system and we looked at the ability of ROM trained at a given Reynolds number ($\mathrm{Re} = 100$) to produce solutions over a range of Reynolds numbers ($\mathrm{Re} \in [60, 150]$). It was shown that the modified bases have both led to an improvement in modeling the flow solutions as one moves in the parameter space. Relatively close to the baseline, the extrapolated and expanded approaches both achieve very good predictions so that using the extrapolated-basis constitutes a better strategy since it does not increase the dimension of the dynamical system while the expanded approach essentially doubles it. However, when considering larger parameter changes, the expanded approach was demonstrated to provide a much more robust strategy. In particular, it was shown that it converges to a stable limit cycle that is a fairly good approximation of the attractor of the full-order simulation even for large parameter changes. This previous study was limited to problems with fixed geometries by considering only value parameters. The present work aims at extending the proposed approaches to shape (or design) parameters (parameters that define the geometry of the fluid domain).

There is a paucity of work in the literature on reduced-order modeling for problems with parameter dependent geometries. Anttonen et al. [16] have looked at the influence of deforming grids on POD-based reduced-order approximations. Similarly to what is observed for value parameters (see e.g. [5,11]), they show that ROMs built at a given set of parameters lose accuracy when applied at a different state. Following a *classical* idea in reduced-order modeling to increase robustness of models (see e.g. [17,6]), they have applied the POD technique to extract a basis from a mixed database that contains snapshots for several different parameter values. They report that the resulting single model is unstable. To circumvent this issue, they have used several ROMs trained for various sets of parameters and switched between them when moving in the shape parameter space. They show that this approach allows for more accurate predictions. However, the cost of the basis selection step is significantly increased since full-order data are required for several parameter values that cover the entire range to be approximated by ROM. This is the most severe limitation because the cost of the reduced-order approach rises dramatically as full-order data are expensive and demanding to obtain. Note that, a similar conclusion holds for value parameters. This limitation can be addressed by building models at each desired state by interpolating POD basis vectors in the parameter space (see e.g. [18,19].) The methodologies presented in this article only requires data at one single state but we use both zero- and first-order information from sensitivity analysis. Note that sensitivity data can be obtained for a fraction of the cost of flow data. We first consider the simple one-dimensional Burgers' equation to introduce and illustrate the proposed methodology to address parameter dependent geometries in reduced-order modeling. Secondly, we investigate the two-dimensional case of laminar flows over a square cylinder in incidence placed in a channel. The shape parameter describes the angular orientation of the cylinder.

The paper is organized as follows; Section 2 deals with the formulation for the direct numerical simulations (DNS) that compute flow and sensitivity data. We use a Lagrangian approach to easily derive the continuous Lagrangian sensitivity equations. For both the one-dimensional Burgers' equation and the two-dimensional Navier–Stokes equations, we derive the weak forms for the primal and sensitivity problems and we introduce the configurations, parameters and appropriate mappings. In Section 3, we first describe the procedure to calculate the POD modes and their Lagrangian sensitivities with respect to shape parameters. Secondly, we present reduced-order models for the Burgers' equation and the Navier–Stokes equations. We also introduce the bases used in these models which are derived using the POD modes and their sensitivities. Finally, Sections 4 and 5 provide extensive numerical results on these low-dimensional approximations and we discuss their ability to predict solutions on parameter dependent geometries.

2. Formulation for the direct numerical simulation

Direct numerical simulation is used to produce accurate full-order data that will be decomposed to generate the spatial basis functions that are employed to define reduced-order approximations. In this study, we are interested in computing solutions to the PDE and their Lagrangian derivatives with respect to shape parameters. This will allow for generating both the POD basis functions and their sensitivities to the design parameters of the problem geometry (known as shape or geometric sensitivities).

There is a wealth of publication on sensitivity analysis that presents the different methodologies to numerically compute shape sensitivities and the interested reader is referred to [13,20] for a broader discussion. We succinctly present here the most popular approaches to compute flow sensitivities:

(1) *Finite-differences of flow solutions:* it is a straightforward approach that only requires evaluations from the flow solver and thus almost no additional development. However, this option is highly costly because the flow solutions must be computed for two or more values of each parameter (see e.g. [21–23].)

(2) *Complex variable method:* it is similar to the finite-difference idea with the exception that a complex perturbation is taken. The first derivatives are obtained by evaluating the imaginary part of the variable at the perturbed state. Thus, the calculation is not affected by round-off errors unlike with finite-differences. However, it does not offer a saving of resources when compared to using finite-differences since the problem must be solved at a perturbed state for each parameter (see e.g. [24–26].)

(3) *Sensitivity equation method (SEM):* The SEMs numerically solve a set of PDEs for the sensitivities. These equations are obtained by differentiation of the (discrete or continuous) flow equations and are thus always linear. Consequently, the SEMs always compute a flow sensitivity for a fraction of the cost of computing the flow making these methodologies very attractive. The differences between SEMs depend on the order of the three operations: mapping, differentiation and discretization [20]. In the continuous sensitivity equation (CSE) approach, the governing equations are first differentiated and then discretized, whereas in the discrete sensitivity equation (DSE) approach, discretization is performed prior to differentiation. One of the main advantages of the DSE approach is that it can be handled through automatic differentiation. It is a powerful approach because the code for calculating sensitivities is almost automatically generated from the code for computing dependent variables (see e.g. [27–29]). However, the CSE method offers a number of advantages over discrete sensitivity algorithms that have been extensively discussed in the literature [30,20]. Among them, we adopt the CSE method here for the two following reasons : First, in the case of shape parameters, the CSE method avoids the delicate issue of evaluating mesh sensitivities. In the present case, because adaptive grids are used, mesh sensitivities do not even exist making the use of DSE method ill-suited. Secondly, the CSE method avoids the differentiation of non-differentiable terms arising from discretization schemes such as limiters, blending functions or stabilization terms.

The general framework and setting of our approach is first introduced in Section 2.1. Then, the methodology is applied and detailed for two different flow problems. First, we consider the one-dimensional Burgers' equation in Section 2.2. Secondly, we address the two-dimensional Navier–Stokes equations in Section 2.3.

2.1. General setting

Let us consider a physical domain Ω_α which depends on a shape parameter α. For each value of α, the physical domain under consideration is changed. In practice, the changes in the domain come from the modification of the boundaries of Ω_α through changes in the parameter α. The classical approach in numerical simulation is to address each value of α separately by considering the corresponding boundaries of Ω_α and meshing the inside domain defined from them. Here, we assume that there exists a mapping $\boldsymbol{\chi}^\alpha$ that maps each material point in Ω_α to a reference domain Ω_0 as illustrated in Fig. 1:

$$\begin{aligned} \boldsymbol{\chi}^\alpha : \quad & \Omega_\alpha \rightarrow \Omega_0 \\ & \mathbf{x}(\alpha) \mapsto \boldsymbol{\chi}^\alpha(\mathbf{x}(\alpha);\alpha) = \xi. \end{aligned} \tag{1}$$

In this setting, the coordinates of a material point in Ω_α, $\mathbf{x}$, depend on α while its coordinates in Ω_0 do not. In practice, since the only relevant physical information on how the domain is affected by changes in α is how the boundaries of Ω_α are altered, there are numerous ways to define the mapping $\boldsymbol{\chi}^\alpha$. In this study, the dependency of the boundaries of Ω_α on α will be simple enough so that their deformations will be limited to *rigid body motion*. Furthermore, we assume that an expression of $\boldsymbol{\chi}^\alpha(\mathbf{x}(\alpha);\alpha)$ is available (more than one hold since the mapping is not uniquely defined). This means that the explicit dependency of $\boldsymbol{\chi}^\alpha$ with respect to α is analytically known. Once a mapping has been chosen, it uniquely maps each point in Ω_α to a point in Ω_0 so that the inverse of this one-to-one onto function exists. It will be denoted $\mathbf{G}^\alpha$ in what follows:

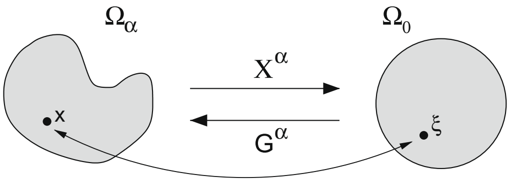

Fig. 1. Mapping from the physical domain to the reference domain.

$$\begin{aligned} \mathbf{G}^{\alpha}: \quad & \Omega_0 \rightarrow \Omega_{\alpha} \\ & \xi \mapsto \mathbf{G}^{\alpha}(\xi;\alpha) = \mathbf{x}(\alpha). \end{aligned} \tag{2}$$

Note that some regularity conditions on $\boldsymbol{\chi}^{\alpha}$ may also be required to properly define the modified problem once expressed in the coordinate system associated to Ω_0 as will be shown for the examples considered in this study.

For more complex geometry and general parameter dependency in practice, analytical or semi-analytical expressions of the mapping will not be available. To address these problems, it is necessary to resort to techniques where the mapping is the solution to an additional problem that is solved numerically along with the PDE at hand. To deal with the deformations of both boundaries and domain, there are two widely used methodologies in the literature. The spring analogy technique considered the existing grid domain as a pseudo-structural system which is governed by the equations of dynamic equilibrium [31,32]. The pseudo-solid approach introduces structural-like equations to manage the deformation of the domain at the continuum level [33,34]. Note that these approaches introduce numerical errors in the definition of the mapping and its gradient.

2.2. One-dimensional Burgers' equation

2.2.1. Primal problem

We first consider the one-dimensional Burgers' equation over the domain $\Omega_{\alpha} = [0, X_m]$:

$$u_{,t} + uu_{,x} - \epsilon u_{,xx} = 0 \quad \text{with} \quad u(x,0) = \begin{cases} 1 & x < \frac{X_m}{2} \\ 0 & x \geqslant \frac{X_m}{2}. \end{cases} \tag{3}$$

and zero Dirichlet boundary conditions at both ends. The mapping of the solution u on Ω_0 will be denoted as $\hat{u}$ in what follows. The values of the solution function are unchanged through the mapping but the distances between material points are since the domains are different. Thus, the gradients with respect to x and ξ are different. It is straightforward to show that the following relations hold:

$$u_{,x} = \hat{u}_{,\xi}\left(\chi^{\alpha}_{,x}\right), \tag{4}$$

$$u_{,xx} = \hat{u}_{,\xi}\left(\chi^{\alpha}_{,xx}\right) + \hat{u}_{,\xi\xi}\left(\chi^{\alpha}_{,x}\right)^2. \tag{5}$$

Hence, the mapped problem defined on the reference domain is:

$$\hat{u}_{,t} + \hat{u}\hat{u}_{,\xi}\left(\chi^{\alpha}_{,x}\right) - \epsilon\left[\hat{u}_{,\xi\xi}\left(\chi^{\alpha}_{,x}\right)^2 + \hat{u}_{,\xi}\left(\chi^{\alpha}_{,xx}\right)\right] = 0 \quad \text{with} \quad \hat{u}(\xi,0) = \begin{cases} 1 & \xi < \chi^{\alpha}\left(\frac{X_m}{2}\right) \\ 0 & \xi \geqslant \chi^{\alpha}\left(\frac{X_m}{2}\right). \end{cases} \tag{6}$$

2.2.2. Sensitivity problem

In this study, sensitivity solutions are obtained by numerically solving the continuous equations for the sensitivity problem. The continuous sensitivity equations are derived formally by implicit differentiation of the primal equations with respect to an arbitrary parameter α. Thus, we treat the variable u as a function of both space/time and parameter α. This dependency is denoted by $u = u(x,t;\alpha)$. For a shape parameter, the coordinates of points in the physical domain Ω_{α}, x, also depend on α. The Lagrangian sensitivity is defined as the total (or material) derivative:

$$S_u = \frac{Du}{D\alpha}. \tag{7}$$

Now, recalling that the coordinates of material points in the reference domain do not depend on α, we take the total differentiation of (6) to yield the continuous Lagrangian sensitivity equation on Ω_0:

$$\begin{aligned} & S_{\hat{u},t} + \left[S_{\hat{u}}\hat{u}_{,\xi} + \hat{u}S_{\hat{u},\xi}\right]\left(\chi^{\alpha}_{,x}\right) + [\hat{u}\hat{u}_{,\xi}]S\left(\chi^{\alpha}_{,x}\right) \\ & -\epsilon\left[S_{\hat{u},\xi\xi}\left(\chi^{\alpha}_{,x}\right)^2 + S_{\hat{u},\xi}\left(\chi^{\alpha}_{,xx}\right) + 2\hat{u}_{,\xi\xi}\left(\chi^{\alpha}_{,x}\right)S\left(\chi^{\alpha}_{,x}\right) + \hat{u}_{,\xi}S\left(\chi^{\alpha}_{,xx}\right)\right] = 0 \end{aligned} \quad \text{with} \quad S_{\hat{u}}(\xi,0) = 0. \tag{8}$$

where $S\left(\chi^{\alpha}_{,x}\right)$ is the sensitivity of the gradient of the mapping. Once, the Lagrangian sensitivity $S_{\hat{u}}$ has been computed on Ω_0, it can be mapped back on Ω_{α} yielding S_u. Note that the boundary conditions for the Lagrangian sensitivity are also homogeneous since the Dirichlet boundary condition for u is unchanged at all material boundary points by parameter changes.

2.2.3. Weak forms of the problems

For both the DNS and the ROM simulations of this problem, the weak form of (6) is formed by a Galerkin projection on a set of suitable test functions $\hat{w}$ that satisfy the homogeneous Dirichlet boundary conditions at the boundary Γ_0 of Ω_0. Here, we assume that the mapping is regular enough so that $\left(\chi^{\alpha}_{,x}\right)^{-1} = G^{\alpha}_{,\xi}$ is well-posed. Then, integration by parts of the term involving $\epsilon\hat{u}_{,\xi\xi}(\chi^{\alpha}_{,x})^2$ yields the following weak form of (6); seek $\hat{u} \in X = H^1(\Omega_0)$ such that $\forall \hat{w} \in X_0 = \{\hat{f} \in H^1(\Omega_0) \mid \hat{f} = 0 \text{ on } \Gamma_0\}$:

$$\int_{\Omega_0} \hat{w}\left[\hat{u}_{,t} + \hat{u}\hat{u}_{,\xi}\left(\chi^{\alpha}_{,x}\right) + \epsilon\hat{u}_{,\xi}\left(\chi^{\alpha}_{,xx}\right)\right] + \hat{w}_{,\xi}\left[\epsilon\hat{u}_{,\xi}\left(\chi^{\alpha}_{,x}\right)^2\right]\, d\Omega_0 = 0. \tag{9}$$

Similar treatments to (8) with integration by parts of the terms involving $S_{\hat{u},\xi\xi}$ and $\hat{u}_{,\xi\xi}$ yield the sensitivity problem in the weak sense; seek $S_{\hat{u}} \in X$ such that $\forall \hat{w} \in X_0$:

$$\begin{aligned}\int_{\Omega_0} \hat{w}\Big[S_{\hat{u},t} + (S_{\hat{u}}\hat{u}_{,\xi} + \hat{u}S_{\hat{u},\xi})\left(\chi^{\alpha}_{,x}\right) + (\hat{u}\hat{u}_{,\xi})S\left(\chi^{\alpha}_{,x}\right) + \epsilon\Big(\hat{u}_{,\xi}S\left(\chi^{\alpha}_{,xx}\right) + S_{\hat{u},\xi}\left(\chi^{\alpha}_{,xx}\right)\Big)\Big] \\ + \epsilon\hat{w}_{,\xi}\left[2\Big(\hat{u}_{,\xi}(\chi^{\alpha}_{,x})S\left(\chi^{\alpha}_{,x}\right)\Big) + S_{\hat{u},\xi}\left(\chi^{\alpha}_{,x}\right)^2\right]\, d\Omega_0 = 0.\end{aligned} \tag{10}$$

Eqs. (9) and (10) are discretized using P_2 isoparametric finite-element and integrated in time using the explicit fourth-order accurate Runge–Kutta scheme.

2.2.4. Parameter and mappings

For this first problem, the shape parameter α is the upper limit X_m of the segment $\Omega_\alpha = [0, X_m]$. Thus, a change in the parameter changes the size of the physical domain. The simplest mapping that can be used is the linear transformation, $\chi^{\alpha}(x, \alpha) = x/\alpha$, that uniformly maps points of Ω_α into $\Omega_0 = [0, 1]$. However, such a simple mapping leads to great simplification of the previous equations (since $\chi^{\alpha}_{,xx} = S(\chi^{\alpha}_{,xx}) = 0$) and hence does not allow for the testing of the whole formulation. Thus, to address more complicated domain deformations, we consider in what follows a quadratic transformation that maps Ω_α to $\Omega_0 = [1, 4]$ from:

$$\chi^{\alpha} : x \mapsto \chi^{\alpha}(x;\alpha) = \left(\frac{x+\alpha}{\alpha}\right)^2, \tag{11}$$

$$G^{\alpha} : \xi \mapsto G^{\alpha}(\xi;\alpha) = \alpha\left(\sqrt{\xi} - 1\right). \tag{12}$$

Note that the points in Ω_0 are uniformly distributed over the segment while points are slightly clustered to the end point in the physical domain due to the quadratic dependency of χ^{α} on x. Finally, the baseline (or reference) state is chosen as $\alpha = \alpha_0 = 1$ which also sets the baseline solution.

2.3. Two-dimensional Navier–Stokes equations

In this section, the methodology is applied to the unsteady incompressible Navier–Stokes equations. Though the derivation of the sensitivity equations is more involved, the essence of the procedure is unchanged. However, we have found it more convenient to take first the weak form of the primal equations, then to map them on the reference domain and differentiate them with respect to the parameter to yield the sensitivity equations. Thus, compare to what has been done for the Burgers' equation, we switch the operation of mapping/differentiation. Though these two ways of proceeding do not lead to the same expressions, they are equivalent. Their discrete solutions should only differ slightly due to differences in numerical approximations.

2.3.1. Primal problem

The pointwise momentum and mass conservation laws are written as:

$$\rho\frac{\partial \mathbf{u}}{\partial t} + \rho(\mathbf{u}\cdot\nabla_x)\mathbf{u} = \nabla_x\cdot\boldsymbol{\sigma}, \tag{13}$$

$$\nabla_x\cdot\mathbf{u} = 0, \tag{14}$$

where $\mathbf{u} = [u, v]^T$ is the velocity vector and $\boldsymbol{\sigma} = (-p\mathbf{I} + \boldsymbol{\tau}(\mathbf{u}))$ is the stress tensor, ρ the density, p the pressure and $\mathbf{I}$ the second-order identity tensor. For Newtonian fluids, the viscous stress tensor is given by:

$$\boldsymbol{\tau}(\mathbf{u}) = \mu\left(\nabla_x\mathbf{u} + (\nabla_x\mathbf{u})^T\right),$$

where μ is the fluid dynamic viscosity. The solution of these equations are sought on a domain Ω_α with a boundary $\Gamma_\alpha = \Gamma^D_\alpha \cup \Gamma^N_\alpha$ and over times $t \in \mathcal{T} \equiv [0, T]$. Dirichlet and homogeneous Neumann boundary conditions are imposed on boundary segments Γ^D_α and Γ^N_α, respectively:

$$\mathbf{u} = \overline{\mathbf{u}} \quad \left(\Gamma^D_\alpha\right), \tag{15}$$

$$\boldsymbol{\sigma}\cdot\mathbf{n} = \mathbf{0} \quad \left(\Gamma^N_\alpha\right), \tag{16}$$

where $\mathbf{n}$ is an outward unit vector normal to the boundary. The variables are initialized in time using a prescribed initial solution.

2.3.2. Weak form of the problem

For both the DNS and the ROM simulations of these PDE, the weak form of Eqs. (13) and (14) are formed by a Galerkin projection on a set of suitable test functions. In particular, the test functions for the momentum equation satisfy the homogeneous version of the Dirichlet boundary conditions Eq. (15) (i.e. $\mathbf{w} \in \mathbf{X_0} = \{\mathbf{f} \in [H^1(\Omega_\alpha)]^2 \mid \mathbf{f} = \mathbf{0} \text{ on } \Gamma_\alpha^D\}$). Then, we seek $\mathbf{u} \in \mathbf{X} = [H^1(\Omega_\alpha)]^2$ and $p \in L_0^2(\Omega_\alpha)$ such that:

$$\int_{\Omega_\alpha} \mathbf{w} \cdot \left[\rho \frac{\partial \mathbf{u}}{\partial t} + \rho(\mathbf{u} \cdot \nabla_x)\mathbf{u}\right] d\Omega = \int_{\Omega_\alpha} p(\nabla_x \cdot \mathbf{w}) - \boldsymbol{\tau} : \nabla_x \mathbf{w} \, d\Omega \quad \forall\, \mathbf{w} \in \mathbf{X_0}, \tag{17}$$

$$\int_{\Omega_\alpha} q(\nabla_x \cdot \mathbf{u}) \, d\Omega = 0 \quad \forall\, q \in L_0^2(\Omega_\alpha). \tag{18}$$

These equations have been obtained by integrating by part the term involving $\boldsymbol{\sigma}$ as classically done:

$$\int_{\Omega_\alpha} (\nabla_x \cdot \boldsymbol{\sigma}) \cdot \mathbf{w} \, d\Omega = \int_{\Gamma_\alpha} (\boldsymbol{\sigma} \cdot \mathbf{w}) \cdot \mathbf{n} \, d\Gamma - \int_{\Omega_\alpha} \boldsymbol{\sigma} : \nabla_x \mathbf{w} \, d\Omega = \int_{\Gamma_\alpha} (\boldsymbol{\sigma} \cdot \mathbf{n}) \cdot \mathbf{w} \, d\Gamma + \int_{\Omega_\alpha} p \, (\nabla_x \cdot \mathbf{w}) - \boldsymbol{\tau} : \nabla_x \mathbf{w} \, d\Omega. \tag{19}$$

The integrand in the boundary integral is zero on Γ_α^D since $\mathbf{w} \in \mathbf{X_0}$ and also on Γ_α^N from the homogeneous Neumann boundary condition Eq. (16). For the DNS, the test functions are finite-element interpolation functions that span $[H^1(\Omega_\alpha)]^2$; for the ROM, the test functions are the POD modes that span a subspace of $[H^1(\Omega_\alpha)]^2$.

2.3.3. Sensitivity problem

To derive the Lagrangian sensitivity equations, we map Eqs. (17) and (18) from Ω_α to Ω_0. It yields:

$$\int_{\Omega_0} \left[\rho \frac{\partial \hat{\mathbf{u}}}{\partial t} + \rho(\nabla_\xi \hat{\mathbf{u}} \cdot \nabla_x \boldsymbol{\chi}^\alpha) \cdot \hat{\mathbf{u}}\right] \cdot \hat{\mathbf{w}} - \hat{p}\, [\nabla_\xi \hat{\mathbf{w}} : \nabla_x \boldsymbol{\chi}^\alpha] + \hat{\boldsymbol{\tau}} : [\nabla_\xi \hat{\mathbf{w}} \cdot \nabla_x \boldsymbol{\chi}^\alpha] \, J \, d\Omega = 0 \quad \forall\, \hat{\mathbf{w}} \in \widehat{\mathbf{X}}_\mathbf{0}, \tag{20}$$

$$\int_{\Omega_0} \hat{q}\, [\nabla_\xi \hat{\mathbf{u}} : \nabla_x \boldsymbol{\chi}^\alpha] \, J \, d\Omega = 0 \quad \forall\, \hat{q} \in L_0^2(\Omega_0), \tag{21}$$

where $\widehat{\mathbf{X}}_\mathbf{0} = \left\{\hat{\mathbf{f}} \in [H^1(\Omega_0)]^2 \mid \hat{\mathbf{f}} = \mathbf{0} \text{ on } \Gamma_0^D\right\}$; J is the Jacobian of the mapping (i.e. the determinant of the matrix associated to the gradient of G^α); and $\hat{\boldsymbol{\tau}} = \mu[\nabla_\xi \hat{\mathbf{u}} \cdot \nabla_x \boldsymbol{\chi}^\alpha + (\nabla_x \boldsymbol{\chi}^\alpha)^T \cdot (\nabla_\xi \hat{\mathbf{u}})^T]$ is the mapped viscous stress tensor.

Implicit total differentiation with respect to the parameter α yields a continuous weak form of the Lagrangian sensitivity problem on the reference domain Ω_0; seek $\mathbf{S}_{\hat{u}} \in \mathbf{X} = [H^1(\Omega_0)]^2$ and $S_{\hat{p}} \in L_0^2(\Omega_0)$ such that:

$$\begin{aligned}
&\int_{\Omega_0} \left\{\hat{\mathbf{w}} \cdot \left[\rho \frac{\partial \hat{\mathbf{u}}}{\partial t} + \rho(\nabla_\xi \hat{\mathbf{u}} \cdot \nabla_x \boldsymbol{\chi}^\alpha) \cdot \hat{\mathbf{u}}\right] - \hat{p}[\nabla_\xi \hat{\mathbf{w}} : \nabla_x \boldsymbol{\chi}^\alpha] + \hat{\boldsymbol{\tau}} : [\nabla_\xi \hat{\mathbf{w}} \cdot \nabla_x \boldsymbol{\chi}^\alpha]\right\} \frac{DJ}{D\alpha} \\
&\quad + \left\{\hat{\mathbf{w}} \cdot \left[\rho \frac{\partial \mathbf{S}_{\hat{u}}}{\partial t} + \rho(\nabla_\xi \mathbf{S}_{\hat{u}} \cdot \nabla_x \boldsymbol{\chi}^\alpha + \nabla_\xi \hat{\mathbf{u}} \cdot S(\nabla_x \boldsymbol{\chi}^\alpha)) \cdot \hat{\mathbf{u}} + \rho(\nabla_\xi \hat{\mathbf{u}} \cdot \nabla_x \boldsymbol{\chi}^\alpha) \cdot \mathbf{S}_{\hat{u}}\right]\right. \\
&\quad \left. - S_{\hat{p}}[\nabla_\xi \hat{\mathbf{w}} : \nabla_x \boldsymbol{\chi}^\alpha] - \hat{p}[\nabla_\xi \hat{\mathbf{w}} : S(\nabla_x \boldsymbol{\chi}^\alpha)] + S(\hat{\boldsymbol{\tau}}) : [\nabla_\xi \hat{\mathbf{w}} \cdot \nabla_x \boldsymbol{\chi}^\alpha] + \hat{\boldsymbol{\tau}} : [\nabla_\xi \hat{\mathbf{w}} \cdot S(\nabla_x \boldsymbol{\chi}^\alpha)]\right\} J \, d\Omega = 0 \quad \forall\, \hat{\mathbf{w}} \in \widehat{\mathbf{X}}_\mathbf{0},
\end{aligned} \tag{22}$$

$$\int_{\Omega_0} \{\hat{q}\, [\nabla_\xi \hat{\mathbf{u}} : \nabla_x \boldsymbol{\chi}^\alpha]\} \frac{DJ}{D\alpha} + \{\hat{q}\, [\nabla_\xi \mathbf{S}_{\hat{u}} : \nabla_x \boldsymbol{\chi}^\alpha + \nabla_\xi \hat{\mathbf{u}} : S(\nabla_x \boldsymbol{\chi}^\alpha)]\} \, J \, d\Omega = 0 \quad \forall\, \hat{q} \in L_0^2(\Omega_0), \tag{23}$$

where the sensitivity of the viscous stress tensor is given by:

$$S(\hat{\boldsymbol{\tau}}) = \mu\left[\nabla_\xi \mathbf{S}_{\hat{u}} \cdot \nabla_x \boldsymbol{\chi}^\alpha + (\nabla_x \boldsymbol{\chi}^\alpha)^T \cdot (\nabla_\xi \mathbf{S}_{\hat{u}})^T + \nabla_\xi \hat{\mathbf{u}} \cdot S(\nabla_x \boldsymbol{\chi}^\alpha) + (S(\nabla_x \boldsymbol{\chi}^\alpha))^T \cdot (\nabla_\xi \hat{\mathbf{u}})^T\right].$$

In these equations, $S(\nabla_x \boldsymbol{\chi}^\alpha)$ is the total derivative of the gradient of the transformation. In practice, the integrands are evaluated on the reference domain so that it is more convenient to only evaluate values of $\mathbf{G}^\alpha$, its gradient and its sensitivity on Ω_0. To do so, we make use of the fact that the mapping has been assumed to possess sufficient regularity so that : $\nabla_x \boldsymbol{\chi}^\alpha = (\nabla_\xi \mathbf{G}^\alpha)^{-1}$ and thus $S(\nabla_x \boldsymbol{\chi}^\alpha) = S((\nabla_\xi \mathbf{G}^\alpha)^{-1})$.

Finally, to properly and completely define the sensitivity problem, initial and boundary conditions must be defined. They are easily derived by taking the total derivative of the flow initial and boundary conditions. We first map the boundary conditions Eqs. (15) and (16) onto the boundaries of Ω_0. From the total differentiation of the latter, one obtains the following boundary conditions for the sensitivity:

$$\mathbf{S}_{\hat{u}} = \mathbf{0} \quad \left(\Gamma_0^D\right), \tag{24}$$

$$-S_{\hat{p}}\, \hat{\mathbf{n}} + S(\hat{\boldsymbol{\tau}}) \cdot \hat{\mathbf{n}} = \mathbf{0} \quad \left(\Gamma_0^N\right). \tag{25}$$

Flows are initialized in time by the solution of the corresponding steady problem modeled by the steady version of Eqs. (20) and (21). Hence, the initial sensitivity condition is the solution of the steady counterpart of Eqs. (22) and (23).

2.3.4. Configurations, parameter and mapping

This study aims at simulating two-dimensional flows over square cylinders at incidence placed in a channel. Full-order simulations of such flows have already been performed in the literature (see e.g. [35,36]). Here, we focus on flows for which the Reynolds number, based on the square edge length D and the inlet velocity U_0, is $\mathrm{Re} = \rho U_0 D/\mu = 100$. We examine configurations that are classified from the angular orientation α of the cylinder with respect to a reference configuration as illustrated in Fig. 2 (the angular orientation of the cylinder with respect to the channel walls is denoted γ). In what follows, the baseline configuration (for which $\alpha = 0$) is obtained for a square cylinder at $\gamma = 22.5^\circ$ of incidence. The parameter space is comprised of all angles for which $\alpha = \alpha_0 \pm \Delta\alpha_{max}$ with $\Delta\alpha_{max} = 22.5^\circ$ so that the configurations range from a square cylinder at zero incidence to 45° of incidence. For this Reynolds number, regardless of the values of the shape parameter α, all flows are reported to be two-dimensional, laminar and T-periodic in time exhibiting a Von Kármán vortex street [36,37]. The vertical distance between the upper and lower channel walls defined the solid blockage ratio β [36]. We consider here $H = 20D$ so that $\beta = D/H = 5\%$ for all configurations. A freestream condition ($\overline{\mathbf{u}} = [U_0, 0]^T$) is prescribed at the inlet. In such a case, it has been shown in the study of Sohankar et al. [36] that the necessary distance for obtaining results independent of the inlet location is about $10D$. Following this direction, the inlet is located $12D$ away from the cylinder front edge. And, the computational domain extends $15D$ away from the rear cylinder edge to allow for the simulation of the transport of several vortexes in the wake of the cylinder. At the outlet of the domain (Γ_N), the homogeneous Neumann boundary condition is applied as described by (16). Finally, the no-slip condition holds on the cylinder and channel walls.

The rotation of the cylinder corresponds to a rigid body rotation R^α of angle α:

$$R^\alpha : \mathbf{x} = \begin{bmatrix} x \\ y \end{bmatrix} \mapsto \begin{bmatrix} x\cos\alpha + y\sin\alpha \\ -x\sin\alpha + y\cos\alpha \end{bmatrix}. \tag{26}$$

To address the sensitivity with respect to α of the flow over the cylinder placed in a channel, the mapping from the physical domain to the reference domain must agree with the rigid body rotation of the cylinder walls while letting all the other boundaries of the domain unchanged since they are unaffected by the cylinder rotation. To do so, we define a function $\hat{\phi} : \Omega_0 \to [0, 1]$ such that:

$$\Delta\hat{\phi} = 0 \quad \text{in} \quad \Omega_0 \quad \text{with} \quad \hat{\phi}(\xi) = \begin{cases} 1 & \text{on } \Gamma_0^{cyl} \\ 0 & \text{on } \Gamma_0 \setminus \Gamma_0^{cyl}, \end{cases} \tag{27}$$

where Γ_0^{cyl} represents the cylinder walls. Hence, by definition this function: (1) returns 1 on the cylinder walls and 0 on the outer boundaries which are the channel walls, inlet and outlet; (2) smoothly varies from 1 to 0 inside the domain according to the Laplace's equation. To derive a suitable space transformation, the mapping is defined by weighting the rigid body rotation by this function as follows:

$$\boldsymbol{\chi}^\alpha : \mathbf{x} = \begin{bmatrix} x \\ y \end{bmatrix} \mapsto \xi = \begin{bmatrix} \xi \\ \eta \end{bmatrix} = \begin{bmatrix} x\cos(\phi\alpha) + y\sin(\phi\alpha) \\ -x\sin(\phi\alpha) + y\cos(\phi\alpha) \end{bmatrix}, \tag{28}$$

$$\mathbf{G}^\alpha : \xi \mapsto \mathbf{x} = \begin{bmatrix} \xi\cos(\hat{\phi}\alpha) - \eta\sin(\hat{\phi}\alpha) \\ \xi\sin(\hat{\phi}\alpha) + \eta\cos(\hat{\phi}\alpha) \end{bmatrix}. \tag{29}$$

Actually, the weighting function could be used to define mappings for any rigid body motion of the cylinder, parameterized by an arbitrary number of parameters as long as the cylinder does not go too close to the outer boundaries. This technique has already been used in the literature to simulate free-surface flows around moving bodies [38]. Fig. 3 illustrates how the resulting domain mapping acts in practice on a computational mesh. Once a mesh of Ω_0 has been generated, one can solve the flow and sensitivity equations for any configuration by selecting the appropriate value of α. Fig. 3(a) shows a close-up

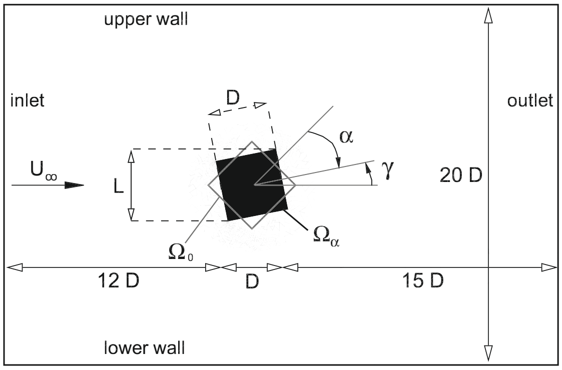

Fig. 2. Problem configuration.

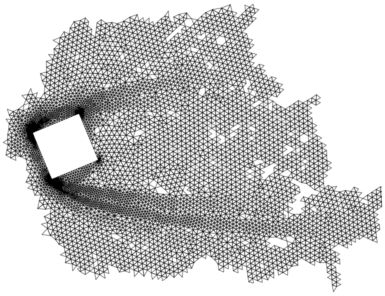

view around the cylinder of such a reference mesh that we have generated by adaptive mesh refinement when solving the steady flow and sensitivity problem for $\alpha = 0$. In this case, the physical domain and mesh match the reference domain and mesh since for $\alpha = 0$, $\boldsymbol{\chi}^{\alpha}$ is simply the identity. Fig. 3(b) shows some isolines of the weighting function $\hat{\phi}$ on the same close-up view. Now, if one wants to compute the flow and sensitivity solutions using the same reference mesh but for other incidences, the actual physical mesh would be different. They are illustrated in Fig. 3(c) and (d) for $\gamma = 45^{\circ}$ and $\gamma = 0^{\circ}$, respectively. These meshes are composed of P2 finite-elements for the flow and sensitivity velocity. Although not illustrated in Fig. 3, note that for the physical meshes the mid-edge nodes are not located at the mid-section of the line segment bounded by two vertexes. Thus, solving Eqs. (17) and (18) on these meshes, as will do for reduced-order models, requires P2-isoparametric elements.

Finally, it is worth noting that the mapping $\boldsymbol{\chi}^{\alpha}$ defined by (28) is *semi-analytical* in the sense that its dependency on α is analytically known but its dependency on the space coordinates is not since ϕ depends implicitly on them.

3. Reduced-order models

3.1. The proper orthogonal decomposition

An important step in reduced-order modeling is to find a suitable set of spatial functions to represent $\mathbf{u}(\mathbf{x}, t) \in \mathbf{X}$ for $t \in \mathcal{T}$. The POD provides such elements by decomposing input data that are comprised of flow solutions from full-order simulations. The main feature of the method is that it converges optimally fast in quadratic mean (i.e. in energy when using the L^2-inner product) compared with any other expansion. That is, the first q POD eigenfunctions capture more kinetic energy in the data on the average than any other set of q orthonormal spatial functions.

We assume that the input collection consists of linearly independent finite-element snapshots, $\mathbf{u}^h(\mathbf{x}, t_i)$, at time instants $t_i \in \mathcal{T}$ for $i = 1, \ldots, m$ and calculated on a mesh with n nodes for a d-dimensional geometry. They are stored in the snapshot data matrix $Y \in \mathbb{R}^{nd \times m}$. Each column of Y represents a single discrete velocity snapshot of the input ensemble. The matrix has full rank due to the linear independence assumption on the snapshots. From the finite-element discretization, the L^2-inner product is computed by the $\mathcal{M}$-inner product: $(\boldsymbol{\psi}, \boldsymbol{\phi})_X = \boldsymbol{\psi}^T \mathcal{M} \boldsymbol{\phi}$ where $\mathcal{M} \in \mathbb{R}^{dn \times dn}$ is the symmetric, positive definite, (generally sparse) finite-element mass matrix. Note that we are using here ϕ for both the finite-element approximation as well as the vector that stores the coefficients of its expansion in the finite-element basis.

The so-called *method of snapshots* introduced by Sirovich [3] consists in finding the temporal eigenfunctions rather than the spatial eigenfunctions (see [4] for details on the relation between these two types of eigenfunctions) because it leads to a much smaller eigenvalue problem:

$$Y^T MY\ V = V\Lambda \quad \text{with} \quad \Phi = YV\Lambda^{-1/2}, \tag{30}$$

where the matrix $\Phi \in \mathbb{R}^{dn\times m}$ collects the finite-element coefficients of the discrete spatial eigenfunctions while $V \in \mathbb{R}^{m\times m}$ collects the temporal eigenfunctions and $\Lambda = \mathrm{diag}(\lambda_1, \ldots, \lambda_m)$. Each column of Φ represents a single POD spatial vector $\boldsymbol{\phi}_j$ and they are ordered such that $\lambda_i \geqslant \lambda_{i+1}$. Due to the assumptions on the FE snapshots, the matrix $B = Y^T MY \in \mathbb{R}^{m\times m}$ is symmetric, positive definite so that the spectral theorem states that (30) exists and the eigenfunctions form a complete real orthonormal set associated to positive eigenvalues. From the physical point of view, λ_k measures the kinetic energy of the data captured by mode k on average over the time interval $\mathcal{T}$:

$$\lambda_k = \frac{V_k^T B V_k}{V_k^T V_k} = \frac{\boldsymbol{\phi}_k^T (YY^T M)\boldsymbol{\phi}_k}{\boldsymbol{\phi}_k^T \boldsymbol{\phi}_k}, \tag{31}$$

where V_k denotes the kth column vector of V.

The POD basis of dimension q is defined as a set of q dominant eigenfunctions. Thus, the subspace $P = \mathrm{span}\{\boldsymbol{\phi}_j\}_{j=1}^{q}$ is the best approximation of dimension q of $\mathrm{span}\{\mathbf{u}^h(\mathbf{x}, t_i)\}_{i=1}^{m}$ in terms of kinetic energy representation. For details the reader is referred to [3,2,4].

3.2. POD mode sensitivity

This section aims at deriving the sensitivity of the discrete POD modes with respect to a generic shape parameter α. They will be used to build bases for reduced-order modeling. Sensitivity analysis of eigenvalue problems has been the subject of several studies in the literature. The methodology for computing the sensitivity of eigenvalues and eigenvectors of multiplicity one is reported in [39,40]. The treatment of general multiple eigenvalues has been examined in [41] and, in the context of structural vibration problems, in [42].

For the present discussion, we consider matrices with simple eigenvalues and we assume that the multiplicity of the eigenvalues is preserved through a change in the parameter.

We start with Eq. (30); then V_k is the solution of the eigenvalue problem:

$$BV_k = \lambda_k V_k. \tag{32}$$

We assume that the components of the B, V and Λ matrices are smooth functions of the parameter α so that each eigenvalue problem can be differentiated with respect to α. Before going any further, we emphasize that there is a number of situations for which this is not true. Indeed, this assumption requires that data snapshots, eigenfunctions and eigenvalues are smooth functions of the parameter in the neighborhood of the current state. As an example, for the case of the flow past a cylinder, the POD modes do not undergo a smooth transition at the first Hopf bifurcation so that the mode sensitivities (with respect to the Reynolds number) are not defined at this Reynolds number. This is a limitation of this method.

For the sake of compactness, the total derivative $(D./D\alpha)$ of any matrix or vector is denoted using the superscript $(^\alpha)$. Thus, implicit differentiation of Eq. (32) with respect to α leads to:

$$(B - \lambda_k I)V_k^\alpha = -(B^\alpha - \lambda_k^\alpha I)V_k. \tag{33}$$

Hence, the sensitivity of the vector V_k is solution to the linear system (33) which has solutions only if the right-hand-side vector belongs to the range of $B - \lambda_k I$. Thus, given that the system matrix is symmetric, V_k must be orthogonal to all the elements of $\ker(B - \lambda_k I)$ which is generated by V_k. In other words:

$$V_k^T (B^\alpha - \lambda_k^\alpha I)V_k = 0. \tag{34}$$

Hence, the sensitivity of the eigenvalues is obtained through:

$$\lambda_k^\alpha = V_k^T B^\alpha V_k. \tag{35}$$

Thus, solutions to system (33) are completely characterized. Note that the same result is obtained by differentiating (31) that expresses λ as the average kinetic energy captured by its eigenvector. We found one particular solution to (33), noted s_k, by seeking the minimum norm least-squares solution. Since λ_k is simple, $s_k + \gamma V_k$ for all $\gamma \in \mathbb{R}$ is the general expression for the solutions to (33). To determine the particular solution that corresponds to the sensitivity of V_k, an additional condition must apply for finding the γ that gives V_k. It naturally comes from the normalization condition $V_k^T V_k = 1$ which already made V_k unique (up to its sign). Differentiating the normalization condition gives $V_k^T V_k^\alpha = 0$ and thus we find:

$$V_k^\alpha = s_k - \left(V_k^T s_k\right)V_k. \tag{36}$$

Note that s_k and thus V_k^α always points in the appropriate direction for any choice in the sign of V_k.

Once the sensitivity of the matrices V and Λ are determined, the sensitivity of the POD spatial modes are easily computed by differentiating $\Phi = YV\Lambda^{-1/2}$:

$$\begin{aligned}\Phi^\alpha &= Y^\alpha V\Lambda^{-1/2} + YV^\alpha\Lambda^{-1/2} + YV(\Lambda^{-1/2})^\alpha \\ &= Y^\alpha V\Lambda^{-1/2} + YV^\alpha\Lambda^{-1/2} - \frac{1}{2}YV(\Lambda^{-1/2}\Lambda^\alpha\Lambda^{-1}) \\ &= Y^\alpha V\Lambda^{-1/2} + YV^\alpha\Lambda^{-1/2} - \frac{1}{2}\Phi\Lambda^\alpha\Lambda^{-1}.\end{aligned} \tag{37}$$

Note that the procedure to compute the sensitivity of the POD modes is exactly the same as the one used for value parameters in [10,11]. However, when performing the differentiation of the matrix B an additional term appears for the case of shape parameters:

$$B^\alpha = (Y^\alpha)^T MY + Y^T MY^\alpha + Y^T M^\alpha Y. \tag{38}$$

Indeed, in the sensitivity of the data, the term $Y^T M^\alpha Y$ accounts for the mesh deformation that is due to the deformation of the physical domain through parameter changes. The sensitivity of the mass matrix is easily obtained from:

$$\begin{aligned}M_{ij}^\alpha &= \frac{D}{D\alpha}\int_{\Omega_\alpha}\varphi_i\varphi_j\, d\Omega = \frac{D}{D\alpha}\int_{\Omega_0}\hat{\varphi}_i\hat{\varphi}_j\, J\, d\Omega \\ &= \int_{\Omega_0}\hat{\varphi}_i\hat{\varphi}_j\,\frac{DJ}{D\alpha}\, d\Omega = \int_{\Omega_\alpha}\varphi_i\varphi_j\,\frac{DJ}{D\alpha}\, J^{-1}\, d\Omega,\end{aligned} \tag{39}$$

where $\{\varphi_j\}_{j=1}^n$ denote the finite-element interpolation functions.

3.3. Reduced-order modeling

Reduced-order modeling revolves around seeking the solution to the PDE at hand in the space spanned by a set of q spatial basis functions $P = \text{span}\{\boldsymbol{\psi}_j\}_{j=1}^q$. Thus, the reduced-order solution $\mathbf{u}^r$ is expressed as a linear combination of these basis functions:

$$\mathbf{u}^r(\mathbf{x}, t) = \mathbf{c}(\mathbf{x}) + \sum_{j=1}^{q}\boldsymbol{\psi}_j(\mathbf{x})a_j(t), \tag{40}$$

where $\mathbf{c}$ is an optional centering trajectory (shift mode). The time dependent coefficients a_j in the combination are obtained by solving the ODE produced by projecting the PDE onto the basis functions. Clearly, the efficiency of this approach crucially depends on the ability of the reduced basis to represent the sought solutions. A truncated POD basis is a good candidate because the POD basis of dimension q is the best approximation of dimension q of the input collection data in terms of kinetic energy representation. However, the best approximation result only holds for the set of parameter values defining the input data. For shape parameters, the POD modes can even be undefined in some regions of some perturbed geometries. Thus, reduced-order solutions for other values of the parameters than the ones used to build the model may be poor approximations of the full-order solutions. This is the main issue of this study and it will be addressed in what follows. For the moment, we build reduced-order models for a basis of dimension q regardless of what are its components. Several different bases will be considered in this study but for all of them we assume that each spatial function satisfies the homogeneous version of the Dirichlet boundary conditions associated to the PDE.

We first build reduced-order models for the one-dimensional Burgers' equation. Here, we do not introduce any centering trajectory in the decomposition u^r, i.e. $c(x) = 0$ in (40). For the sake of simplicity, equations are written on the physical domain Ω_α. Hence, we seek $u^r \in P$ such that $\forall\psi_i \in P$:

$$\int_{\Omega_\alpha}\psi_i\left[u^r_{,t} + u^r u^r_{,x}\right] + \epsilon\psi_{i,x}u^r_{,x}\, d\Omega_\alpha = 0. \tag{41}$$

For the Navier–Stokes equation, we consider the averaging operator which is the arithmetic average to define the shift mode $\mathbf{c}(x) = \langle\mathbf{u}^h(x,t)\rangle = \frac{1}{m}\sum_{k=1}^m\mathbf{u}^h(x,t_k)$ so that the POD will be applied to the data $\mathbf{y}_i^h(x) = \mathbf{u}^h(x,t_i) - \mathbf{c}(x)$. However, we assume that each basis vector is divergence-free. Hence, taking $\mathbf{w} = \boldsymbol{\psi}_i$ for $i = 1, 2, \ldots, q$ in Eqs. (17) and (18), one obtains:

$$\int_{\Omega_\alpha}\left[\rho\frac{\partial\mathbf{u}^r}{\partial t} + \rho(\mathbf{u}^r\cdot\nabla_x)\mathbf{u}^r\right]\cdot\boldsymbol{\psi}_i\, d\Omega = -\int_{\Omega_\alpha}\tau(\mathbf{u}^r) : \nabla_x\boldsymbol{\psi}_i\, d\Omega. \tag{42}$$

Note that the incompressibility constraint (18) is automatically satisfied since the $\boldsymbol{\psi}_j$ are solenoidal in the decomposition (40), and its associated Lagrange multiplier, the pressure, is eliminated from (17).

Using the decomposition (40) in the set of q Eqs. (41) or (42) leads to a set of ODE for the time coefficients $\mathbf{a} = [a_1, \ldots, a_q]^T$:

$$C\dot{\mathbf{a}}(t) = f(\mathbf{a}(t)) \quad \forall t \in [0, T], \tag{43}$$

where $C_{ij} = (\boldsymbol{\psi}_j, \boldsymbol{\psi}_i)_X$ which is the identity matrix for orthonormal bases. In the present study, these ODE are integrated in time using either the implicit second-order Crank–Nicolson scheme or the explicit forth-order Runge–Kutta scheme. Finally, initial conditions can be obtained from available DNS data. For an orthonormal basis, one has: $a_i(0) = (\mathbf{y}(0,\cdot), \boldsymbol{\psi}_i(\cdot))_X$ for $i = 1, 2, \ldots, q$.

3.4. Bases used in ROM for parameter dependent geometry

To produce reduced-order solutions at perturbed states for $\alpha = \alpha_0 + \Delta\alpha$, we first considered the following bases:

- *Baseline POD basis*: This is the traditional approach in ROM where the POD basis built from the data at the baseline state α_0 is used in (40) to subsequently produce reduced-order models at perturbed states α. These spatial modes are only available on the baseline geometry but they can easily be mapped on the perturbed geometry using the transformation defined in Sections 2.2.4 and 2.3.4. Note that in classical fully-Eulerian approaches used in DNS, no mapping is available.
- *Perturbed POD basis*: the reduced-order model is constructed by using the POD modes extracted from the solution data obtained by a DNS at the perturbed state α. This is a costly approach since each new reduced-order simulation at a perturbed state requires DNS data at this state. Thus, it has little interest in practice but will be used in the remainder of this study as a reference low-dimensional solution.

Following previous studies for value parameters in [10,11], we examine two different ideas for constructing improved reduced-bases using the Lagrangian sensitivity of the POD modes at the baseline state:

- *Extrapolated basis*: we treat each POD mode as a function of both space and parameter α : $\boldsymbol{\phi} = \boldsymbol{\phi}(\mathbf{x}; \alpha)$. A change $\Delta\alpha$ is reflected in the modes through a first-order expansion in the parameter space:

$$\boldsymbol{\phi}(\mathbf{x}; \alpha) = \boldsymbol{\phi}(\mathbf{x}; \alpha_0) + \Delta\alpha \frac{D\boldsymbol{\phi}}{D\alpha}(\mathbf{x}; \alpha_0) + O(\Delta\alpha^2). \tag{44}$$

  The capability of this extrapolation clearly depends on whether or not the POD modes exhibit a nearly linear dependency with respect to the parameter α. However, the dimension of the reduced basis is preserved and the reduced approximation of the solution variables still expressed using (40). Once again, the spatial functions are only available on the baseline geometry over which they have been computed but they are mapped on the perturbed geometry. This is a natural way to proceed given that the extrapolation is performed using Lagrangian sensitivities.
- *Expanded basis*: the sensitivities of the modes can be shown to span a different subspace than the POD modes (see e.g. [10]). Thus, it is natural to expect that if the approximated solution is selected in the union of the two subspaces generated by the POD modes and their sensitivities a broader class of solutions can be represented. It amounts to expand the baseline basis constituted of the first q eigenfunctions with their q sensitivities: $[\phi_1; \ldots; \phi_q; \phi_1^\alpha; \ldots; \phi_q^\alpha]$. The underlying assumption behind this approach is that the subspace spanned by the mode sensitivities is well-suited to address changes in solutions induced by a change in the parameter. However, the dimension of the reduced basis has doubled and the reduced approximation of the flow variables is now expressed from:

$$\mathbf{u}^r(\mathbf{x}, t) = \mathbf{c}(\mathbf{x}) + \sum_{j=1}^{q} \boldsymbol{\phi}_j(\mathbf{x}) a_j(t) + \sum_{j=q+1}^{2q} \boldsymbol{\phi}_{j-q}^{\alpha}(\mathbf{x}) a_j(t). \tag{45}$$

It is worth noting that, once mapped on any perturbed physical domain, all the bases presented above can be used in (41) and/or (42) as a set of trial functions since both the POD eigenfunctions and their sensitivities satisfied the homogeneous Dirichlet boundary condition of the PDE at hand. However, in the case of the Navier–Stokes equations, the semi-analytical mapping presented in Section 2.3.4 does not preserve *incompressibility*. That is, solenoidal spatial functions (as the baseline POD modes and their sensitivities) will no longer be divergence-free once mapped on any other geometry than the one on which they have been computed. There is no easy way to derive a mapping that would preserve this property. As a consequence, (42) is no longer exactly valid when considering mapped modes because the pressure term cannot be fully eliminated from (17). However, based on our experience, it has little influence in practice. This is because the departure from the divergence-free condition is limited even for large parameter perturbations (note that due to the finite-element method, unmapped modes are only solenoidal in the weak sense and not in a pointwise manner). In particular, the pressure term in (17) remains small compare to the other ones and can be neglected. It is worth noting that these comments are based on the authors' own experience and we do not claim that they will be valid for all situations nor that a general result is available.

4. Numerical results for the 1D Burgers' equation

4.1. DNS solution and sensitivity data

The computational domain is comprised of 201 nodes and the equations are integrated over the time interval [0,1] with 4800 integration steps for a viscous coefficient $\epsilon = 0.01$. Fig. 4 shows the baseline solution and its Lagrangian sensitivity with respect to α at three different times. The evolution of the solution in time is characterized by a falling wave over the left half of the domain and a traveling wave over the right half of the domain [15]. To check the accuracy of the Lagrangian sensitivity obtained by the sensitivity equation method (we refer to it as SEM), we compare it to the sensitivity computed by second-order centered finite-difference (FD) of two solutions with step $\Delta\alpha = 0.001$:

$$\frac{Du}{D\alpha}(x(\alpha_0);\alpha_0)\bigg|_{FD} = \frac{u(x(\alpha_0+\Delta\alpha);\alpha_0+\Delta\alpha) - u(x(\alpha_0-\Delta\alpha);\alpha_0-\Delta\alpha)}{2\Delta\alpha}. \tag{46}$$

Note that since we consider Lagrangian sensitivity we do not face the issue of non matching meshes as it is the case for Eulerian sensitivities [14]. Note also that the FD step $\Delta\alpha$ has been chosen sufficiently small for the FD to be accurate and sufficiently large for the difference between the two nearby flow solutions to be at least one order of magnitude larger than the discretization error (this holds whenever FD approximations are used throughout this article). As can be seen in Fig. 4, the agreement between the sensitivities calculated by the two approaches is very good. This validates the methodology used to produce Lagrangian sensitivity data.

4.2. Shape sensitivity of the POD

From these solutions, $m = 60$ snapshots of the finite-element solution and sensitivity were collected to assemble the snapshot data matrix Y and its sensitivity Y^{α}. The fluctuant kinetic energy captured by the POD modes is illustrated by plotting the POD spectrum in logarithmic scale in Fig. 5 for the first 40 eigenvalues. Observe that there is a rapid decrease in the energy distribution for all parameter values. Furthermore, as can be seen in Fig. 5(b) which shows the POD spectra obtained from the decompositions of the solution data at some perturbed states (the dash-dotted line corresponds to the baseline), the lower the value of α, the steeper the slope of the spectrum and thus the better the efficiency of the POD. This phenomenon

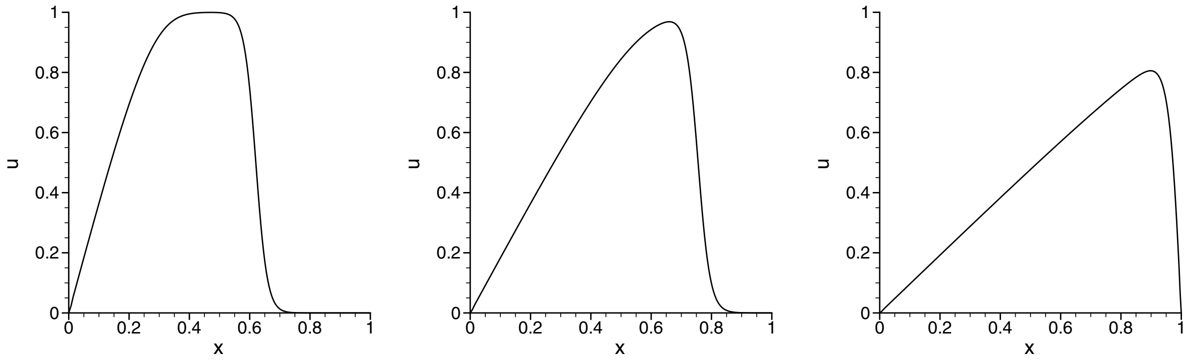

(a) Solution at time 0.2373 (b) Solution at time 0.5085 (c) Solution at time 1

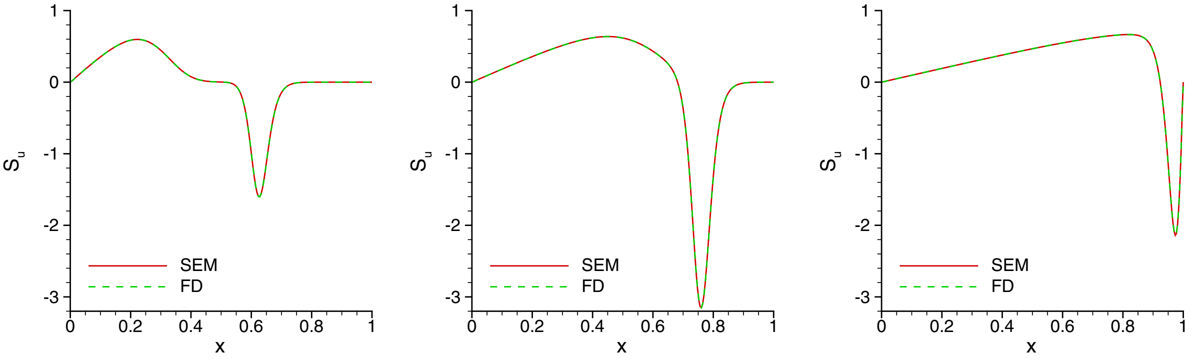

(d) Sensitivity at time 0.2373 (e) Sensitivity at time 0.5085 (f) Sensitivity at time 1

Fig. 4. Solution and Lagrangian sensitivity of the Burgers' equation.

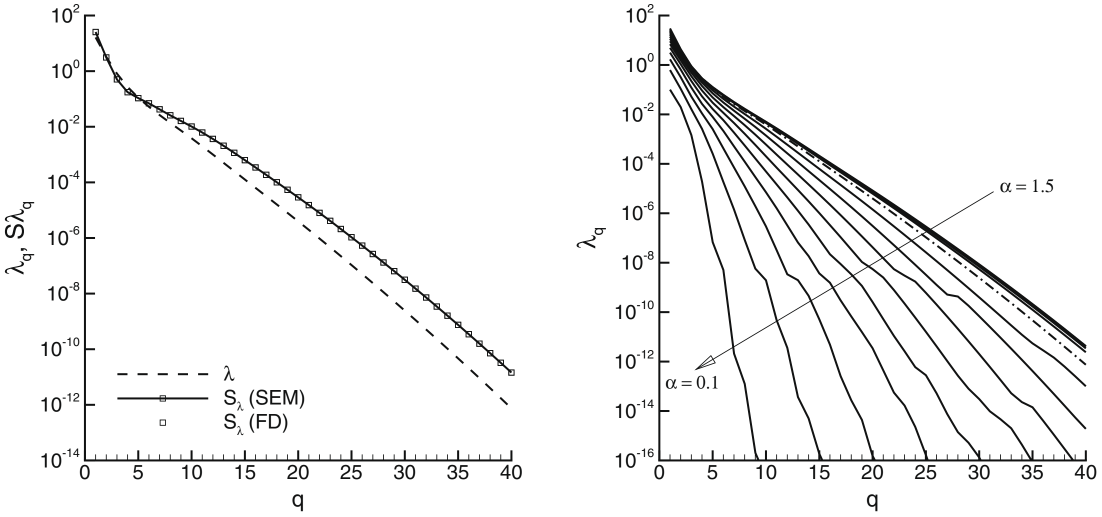

(a) POD spectrum and its sensitivity at $\alpha = 1$ (b) POD spectra for $\alpha = 0.5$ to 1.5 every $\Delta\alpha = 0.1$

Fig. 5. POD spectra for solutions to the Burgers' equation.

saturates for the largest parameter values. However, it means that a POD basis of fixed dimension q accounts for a more important fraction of the energy in the data when α is small. Hence, it is expected that a q-dimensional POD-Galerkin models will be more accurate when α is small. Fig. 5(a) also shows the sensitivity of the POD spectrum as computed from the solution and sensitivity data by (35) at the baseline state. We compare them to the sensitivity of the eigenvalues computed by centered finite-difference (see Eq. (46)) using the decompositions of two perturbed datasets. As can be seen, the agreement between the two approaches is very good. Note that the eigenvalue sensitivity decreases with the mode number in a similar way as the eigenvalues do. This shows that the ordering of the eigenvalues will be preserved through changes in the shape parameter. Note also that all the eigenvalue sensitivities are positive so that an increase in the parameter will bring an increase in the eigenvalues, and conversely, as confirmed by the spectra in Fig. 5(b). Finally, the order of magnitude of the eigenvalue sensitivities is similar to that of their corresponding eigenvalues but the relative, or normalized sensitivities (S_{λ_k}/λ_k) increases with the mode number k. This means that a change in the parameter will have more relative effect on the higher mode eigenvalues than on the lower ones. Hence, a positive perturbation of the parameter will decrease the steepness of the spectrum, and conversely. All these results show that the sensitivity information is very useful in predicting the behavior of the flow and its characteristics with respect to a parameter at a given state.

Fig. 6 presents the first three POD modes and their sensitivities extracted at the baseline and Fig. 7 the next three components. Again, in these figures the mode sensitivities are compared to those obtained by finite-difference showing a very good agreement. This validates the methodology presented in Section 3.2 to calculate the POD mode sensitivities for shape parameters. Note that there is a lot of structures in the POD basis functions over the left half of the domain [0, 0.5] while the right half [0.5, 1] is primarily Fourier modes that become more and more oscillatory as the mode number increases. This reflects the fact that the main feature in the evolution of the solution over the right half of the domain is a traveling wave. Note also that the mode sensitivities exhibit steep variations close to the left end and around the mid-section of the domain. There are due to the discontinuities in the initial solution of the Burgers' equation that are rapidly smeared out by the viscous term.

4.3. Reduced-order model predictions

We now examine the accuracy of the reduced-order models built using the bases presented in Section 3.4. Considering ±20% and ±50% changes in the shape parameter, we examine the following cases:

1. $\Delta\alpha = +0.2: \ \alpha = 1.2$ so that $\Omega_\alpha = [0, 1.2]$,
2. $\Delta\alpha = -0.2: \ \alpha = 0.8$ so that $\Omega_\alpha = [0, 0.8]$,
3. $\Delta\alpha = +0.5: \ \alpha = 0.5$ so that $\Omega_\alpha = [0, 1.5]$,
4. $\Delta\alpha = -0.5: \ \alpha = 1.5$ so that $\Omega_\alpha = [0, 0.5]$.

For each case, we compare the low-order solutions u^r to the full-order solution obtained by DNS at the perturbed state $u^{DNS}|_\alpha$ in Figs. 8 and 9. The error in u^r is measured as:

$$\text{error}(\alpha) = \langle \|u^r - u^{DNS}\|_X \rangle|_\alpha = \int_0^1 \sqrt{\int_{\Omega_\alpha} (u^r - u^{DNS})^2|_\alpha \, d\Omega_\alpha} \, dt \tag{47}$$

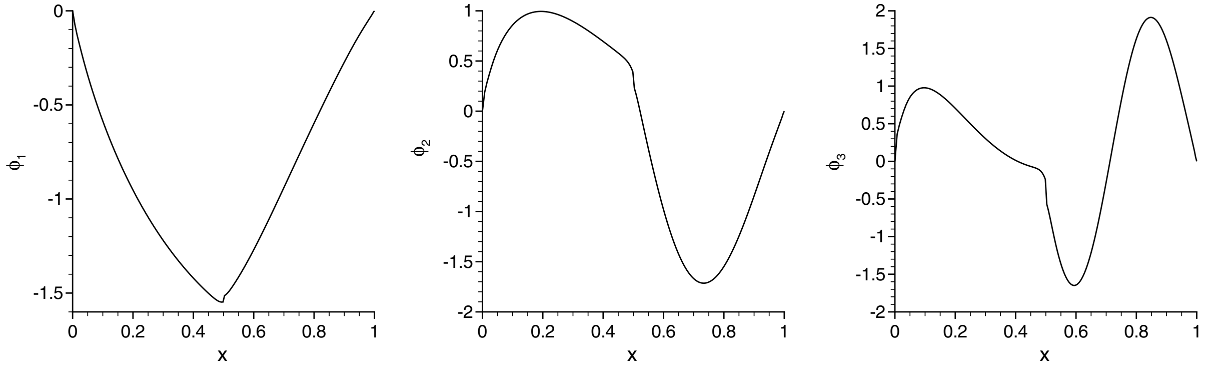

(a) ϕ_1 (b) ϕ_2 (c) ϕ_3

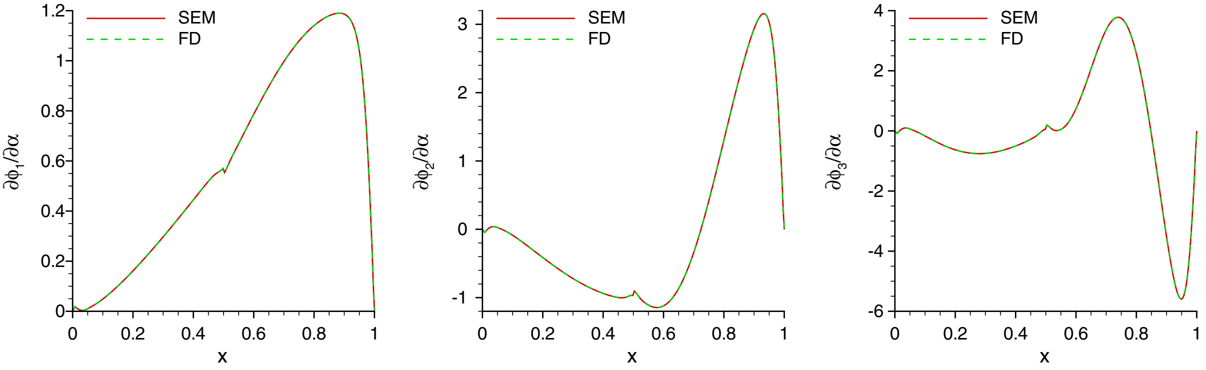

(d) $\frac{D\phi_1}{D\alpha}$ (e) $\frac{D\phi_2}{D\alpha}$ (f) $\frac{D\phi_3}{D\alpha}$

Fig. 6. Modes 1, 2 and 3 and their Lagrangian sensitivities.

We first focus on the results for negative changes in the parameter shown in Fig. 8. For the vast majority of the cases, the ROM based on the recomputed POD basis at the current state performs best as expected. As already stated, this is not a practical approach since it requires high computational cost to obtain DNS data at each and every perturbed state. However, the error in this modeling increases for the largest basis dimensions. This is because the highest order modes contain no relevant physical information but only random, highly oscillatory, *numerical* noise. Indeed, as can be seen in Fig. 5(b), for $\alpha = 0.5$ the values of λ_q reach the machine floating point (double-)precision for q around 30. This means that the discrete data at this state are *exactly* reproduce up the machine precision with the first 30–35 POD modes only. Thus, the last 25–30 modes are *randomly* determined by non-significant digits in the data (note that this effect may have been delayed or mitigated if a finer mesh had been used). These physically irrelevant and oscillatory modes, when included in the ROM bases, introduce numerical imprecision in the matrices which subsequently spoil the global reduced-order solutions. Hence, these modes should just be discarded.

However, the traditional approach in reduced-order modeling, which uses the baseline POD modes, performs poorly. As expected, the larger the parameter perturbation, the larger the error in this modeling. The two approaches relying on the mode sensitivities provide interesting alternatives that bring about significant improvements. For low-dimensional bases and small parameter perturbations, the first-order extrapolation of the POD modes in the parameter space constitutes the best idea. Indeed, for $\Delta\alpha = -0.2$, the ROM from the extrapolated-basis and the perturbed basis perform similarly up to a dimension of 10–12. This result indicates that the first POD modes still depend almost linearly on the shape parameter for a 20% negative perturbation in the parameter. However, the saturation in the decrease of the error with the basis dimension occurs sooner when using the extrapolated-basis than for the recomputed basis. The further from the baseline, the sooner it happens. For a 50% negative perturbation in the parameter, the error in the model built from the extrapolated-basis is much larger than what is obtained when using the perturbed POD but still smaller than for the baseline POD. However, solutions from the ROMs built using the expanded bases are as accurate as solutions from the models built from the recomputed POD at the perturbed states. This is even true for a 50% negative perturbation in the parameter. At this point this is important to recall that the dimension of the expanded model is twice as large as the number q of (baseline, extrapolated or perturbed) POD modes in the other approaches (see (45)) but only uses baseline data.

We now focus on the results for positive changes in the parameter shown in Fig. 9. As can be seen, the expanded approach performance are slightly worse than previously but still provides a much better approximation than the baseline approach.

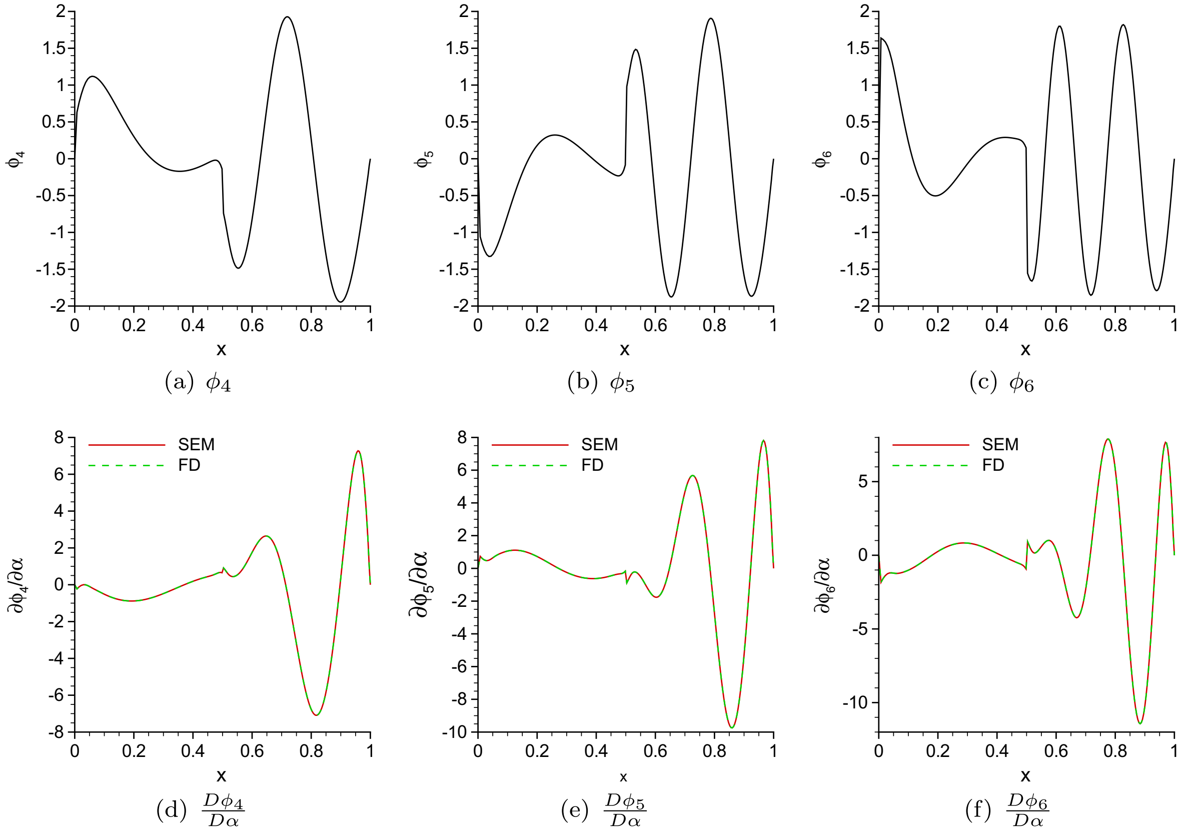

(a) ϕ_4 (b) ϕ_5 (c) ϕ_6

(d) $\frac{D\phi_4}{D\alpha}$ (e) $\frac{D\phi_5}{D\alpha}$ (f) $\frac{D\phi_6}{D\alpha}$

Fig. 7. Modes 4, 5 ,6 and their Lagrangian sensitivities.

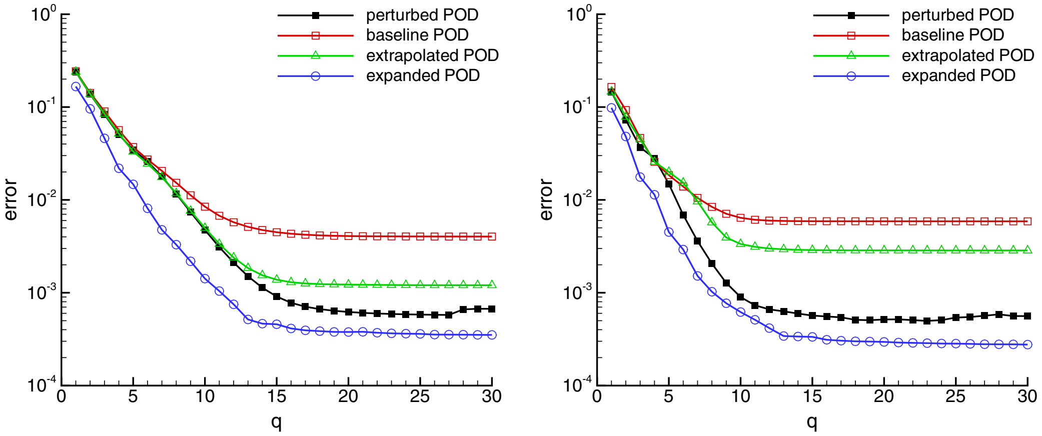

(a) ROM at $\alpha = 0.8$ ($\Delta\alpha = -0.2$) (b) ROM at $\alpha = 0.5$ ($\Delta\alpha = -0.5$)

Fig. 8. Error in reduced-order solutions as a function of q for $\Delta\alpha < 0$.

However, on this side of the baseline state, the error in the extrapolated-basis models is larger than the one in the baseline basis models. It shows that the extrapolation of the POD modes in the parameter space up to +20% or +50% is not a good approximation of the POD modes at the perturbed states. Hence, the linear dependency of the POD modes with respect to the parameter is only valid close to the baseline for positive parameter changes. It contrasts with previous conclusion drawn for negative parameter changes. These results highlight the local nature of this approach that can be limited when the dependency of the POD modes to a parameter is complex.

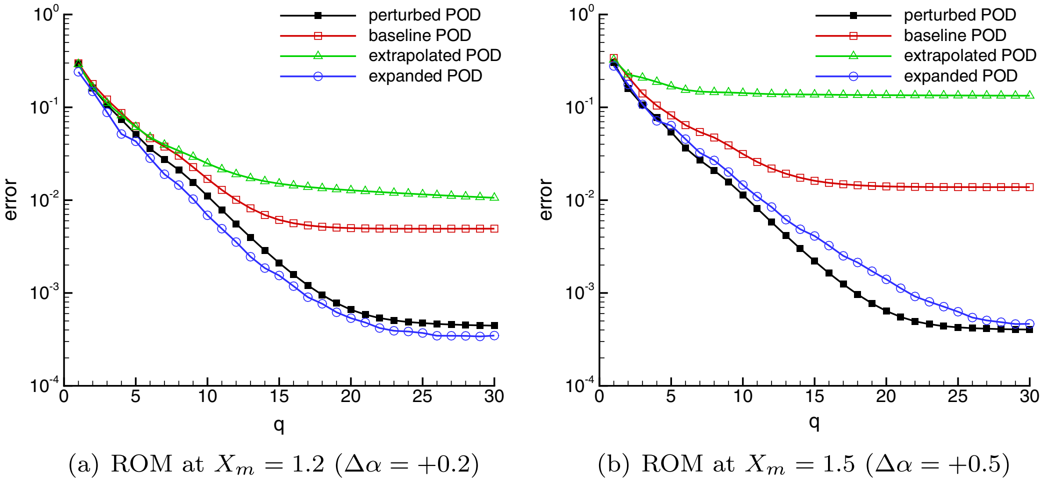

(a) ROM at $X_m = 1.2$ ($\Delta\alpha = +0.2$) (b) ROM at $X_m = 1.5$ ($\Delta\alpha = +0.5$)

Fig. 9. Error in reduced-order solutions as a function of q for $\Delta\alpha > 0$.

It is worth noting that the low-index modes exhibit a more linear dependency than the high-index ones: (1) at a given parameter perturbation, the first extrapolated modes are closer to their perturbed counterparts; (2) an almost linear dependency is preserved further from the baseline for low-index modes than for the high-index ones. A general result cannot be stated but this tendency has been observed in all the cases and parameters we have studied up to now, here and in previous studies. Thus we report that the more energy is contained in a mode, the more likely it is to depend linearly on parameters. This is an important result for the sensitivity-based reduced-order model since the most energetic modes are expected to play the most important role in a dynamical system (though it might not always be true). This explains why the extrapolated approach performs similarly to the perturbed approach for the lowest basis dimensions. However, here, the linear dependency around the baseline state is much better for negative perturbations than for positive perturbations. This is the main reason why the sensitivity-based approaches yields more accurate solutions for negative perturbations. Furthermore, as stated previously, positive perturbations lead to smoother spectra and thus decompositions for which a smaller fraction of the energy is contained in the low-index modes that exhibit a better linear dependency.

Finally, the contrast between the results for positive and negative perturbations can also be partly explained from the data themselves. They consist of the baseline solution snapshots collected in the time interval $[0,1]$. Once the data have been decomposed, the POD modes reflect the information contained in the snapshots and a part of it may be useless to model solutions at some perturbed states. Here, the solution is characterized by a traveling wave and a falling wave. The baseline snapshots provide information on these waves that are relevant and needed to approximate solutions at any state. However, after a sufficiently long-time, the traveling wave, which moves from the left to the right, reaches the right end of the domain and is stopped by the zero Dirichlet boundary condition. Later, the front of the wave, associated to large velocity gradient, is intensely damped out by the viscosity while a larger and larger fraction of the fluid is brought in this area to be subsequently slowed down to rest. As can be seen in Fig. 4(c), this phenomenon has already started prior to the final integration time for the baseline configuration and is represented in the baseline data and hence in the baseline POD modes and their sensitivities. Since the initial traveling wave speed is the same for all configurations, this phenomenon always occurs for negative parameter perturbations that reduce the domain size. However, for sufficiently large positive parameter perturbations, the traveling wave does not reach the left end of the perturbed domain in the time interval $[0,1]$. Indeed, for $X_m = 1.2$ this process has hardly started and simply does not occur for $X_m = 1.5$. Hence, the spatial modes extracted at the baseline state contain informations that are useless to model the perturbed solutions. It would have been better to collect the same number of baseline snapshots over a shorter time interval thus providing more details about the relevant physical processes for these perturbed solutions. Note that the worse scenario would have been to extract spatial modes from data containing no information on this final process, say at $X_m = 1.5$ over the time interval $[0,1]$, to model solutions for which it takes place, say at $X_m = 1$ over the same time interval.

We now look at the error as calculated from Eq. (47) for a set of perturbations in the parameter ranging from +0.5 to -0.1. Fig. 10(b), (d) and (f) present the errors in u^r for bases of dimension 4, 10 and 20, respectively. We also present the error in reduced-order solutions whose time coefficients have been obtained by projection on the DNS data at perturbed states. That is, for a basis comprising q spatial function ψ_i, we consider the reduced-order approximation

$$u^p(x,t) = \sum_{j=1}^{q} \psi_j(x) a_j^p(t), \tag{48}$$

where the a_i^p are obtained by solving the linear system:

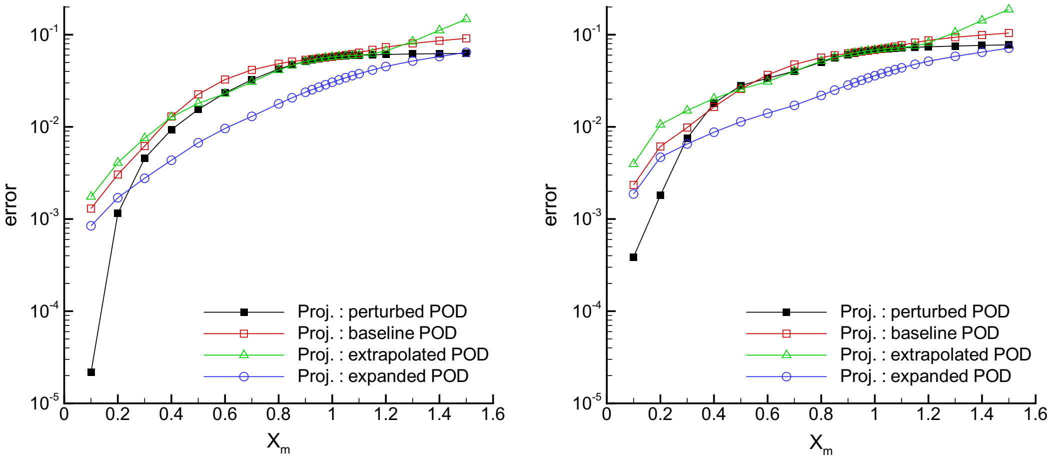

(a) Projection on the perturbed data for $q = 4$ (b) ROM for $q = 4$

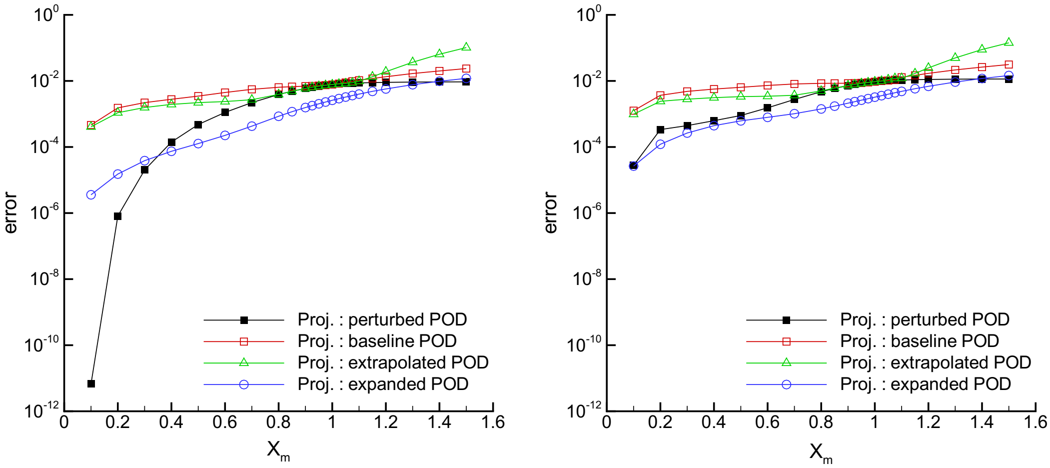

(c) Projection on the perturbed data for $q = 10$ (d) ROM for $q = 10$

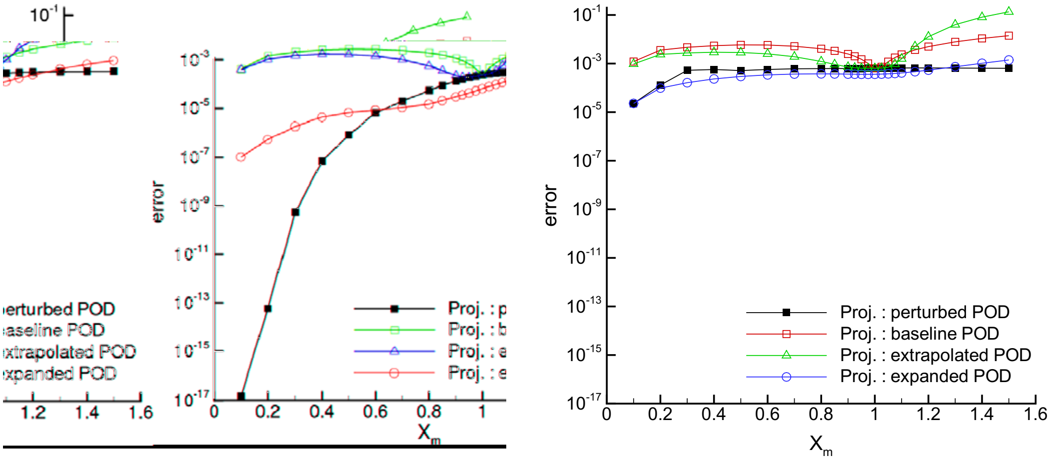

(e) Projection on the perturbed data for $q = 20$ (f) ROM for $q = 20$

Fig. 10. Error in reduced-order solutions as a function of α.

$$\forall i,j = 1,2,\ldots,q \quad \int_{\Omega_\alpha} u^{DNS}|_\alpha(x,t)\psi_i(x)\ d\Omega_\alpha = a_j^p(t)\int_{\Omega_\alpha}\psi_j(x)\psi_i(x)\ d\Omega_\alpha.$$

The error in u^p indicates how good a given basis is to approximate the data at a given state while the error in u^r indicates how appropriate a given basis is to approximate the dynamic of the solution at a given state. While these errors are not totally uncorrelated, they measure different properties of the bases.

Fig. 10(a), (c) and (e) present the errors in u^p for bases of dimension 4, 10 and 20, respectively. We first notice that the smaller the domain size, the smaller the error associated to the recomputed POD at the perturbed states. Again, this is due to the fact that the more reduced is the size of the domain, the more energy is contained in the first q POD modes. When considering the perturbed POD, it is also clear that errors in u^p are always smaller than the ones in u^r since it is less *demanding* for a given basis to approximate some flow data than to predict the flow dynamics.

In a restricted area around the baseline, the extrapolated approach matches the perturbed approach results showing how far in the parameter space the modes exhibit a linear dependency. The agreement between the two approaches holds on a larger range of parameter values for $q = 10$ than for $q = 26$. This confirms that the low-index modes exhibit a more linear dependency on the parameter than the high-index ones. When going further from the baseline, the disagreement between the extrapolated-basis modeling and the perturbed-basis modeling increases. For positive parameter perturbations, this increase soars so that the error in the extrapolated approach becomes larger than for the baseline approach. However, the expanded approach leads to limited errors over the whole range of parameter values.

5. Numerical results for the 2D Navier–Stokes equations

5.1. Flow DNS data

To validate the present DNS results, we compare the Strouhal number St, the mean drag coefficient $\overline{C_D}$ and the mean lift coefficient $\overline{C_L}$ obtained for several incidences to the numerical results of Sohankar et al. [36] in Fig. 11. For the purpose of this comparison, and only in this section, all geometrical lengths are scaled with d, the projected width of the cylinder in the streamwise direction $d/D = \cos\gamma + \sin\gamma$. For example, the Reynolds number is defined as $\mathrm{Re} = \rho U_0 d/\mu$ and the Strouhal number as $St = f_s d/U_0$ where f_s is the shedding frequency. As a consequence, the fluid viscosity is changed with the incidence γ to keep the Reynolds number at 100 for all simulations. This is in contrast with what has been presented in Section 2.3.4 where all geometrical lengths are scaled with D, the cylinder diameter. The use of d as a reference length is only valid for this section to compare results with those of Sohankar et al.

As can be seen in Fig. 11, the agreement is quite good which validates the present numerical approach. The small discrepancies with the results published in [36] are due to differences in numerical techniques and grid point distributions.

5.2. Sensitivity DNS data

Fig. 12 shows the baseline drag and lift sensitivities with time. As previously, one can compare in this figure the SEM sensitivities to centered finite-difference approximations calculated for $\Delta\alpha = 10^{-5}$ *rad* to assess the accuracy of the sensitivity data. Note that though a periodic state is reached for the flow, the sensitivity signals still grow in time and always will since as time advances the departure of any perturbed flow from the baseline flow becomes larger and larger.

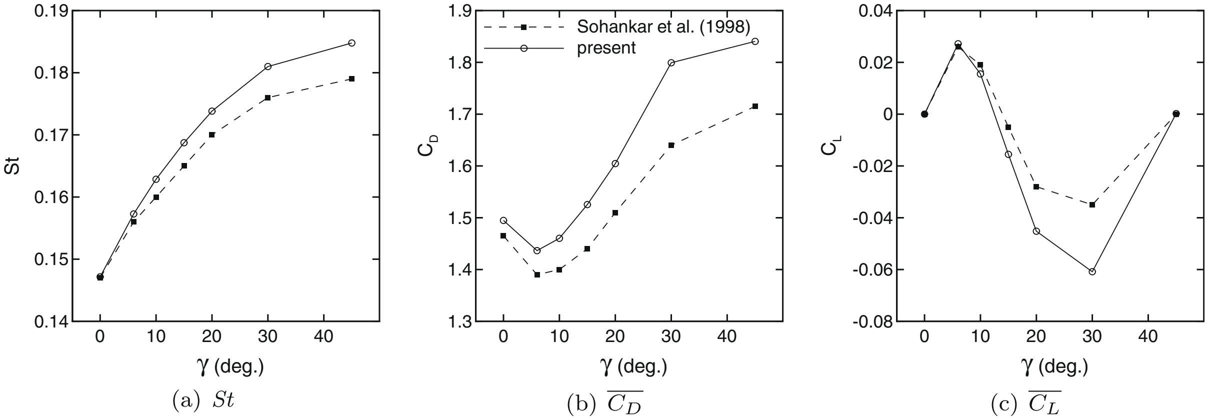

(a) St (b) $\overline{C_D}$ (c) $\overline{C_L}$

Fig. 11. Validation of flow DNS data.

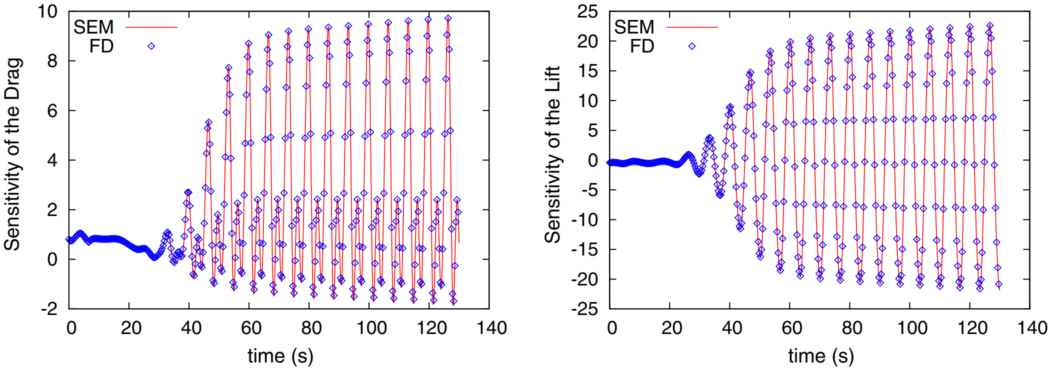

(a) Sensitivity of the drag (b) Sensitivity of the lift

Fig. 12. Flow sensitivity at the baseline state: comparison between FD and SEM approaches.

5.3. POD modes and their Lagrangian sensitivities

During one vortex shedding cycle of period T, $m = 60$ snapshots of the FE solutions (flow and sensitivity) were collected to build the snapshot data matrix and its sensitivity. The fluctuating kinetic energy captured by the POD modes is illustrated by plotting the POD spectra on a logarithmic scale in Fig. 13 for three different configurations. There is a rapid decrease in the energy distribution so that the effectiveness of the POD is rapidly large. Indeed, the first six POD modes account for more than 99% of the flow energy for all configurations. Note also that the square cylinder incidence has little influence on the POD spectrum which remains qualitatively the same for all parameter values. However, the change in the spectrum is more important for negative parameter perturbations than for positive ones. The lower the value of α, the sharper the spectrum.

Fig. 14(a) shows the values of the Lagrangian sensitivity of the POD eigenvalues. For verification purposes, we compare them to the sensitivity computed by finite-differences again for $\Delta\alpha = 10^{-5}$ *rad*. As can be seen, the agreement between the two approaches is very good. Except for the fifth and sixth modes, the eigenvalue sensitivity (roughly) decreases with the mode number in a similar way as the eigenvalues do. This shows that the ranking of the eigenvalues will be preserved through changes in the parameter. Only the rate of the energy decay will be affected. Note that all these results are confirmed by the spectra shown in Fig. 14(a) showing how sensitivity can be used to characterize flow solutions in the parameter space. To assess the accuracy of the POD spatial mode sensitivities, Fig. 14(b) compares the norm of the first 30 POD mode sensitivities with their FD counterparts. We observe that the agreement is very good.

Fig. 15 shows the contours of the streamwise and normal components of the first four spatial POD vectors at the baseline. In this figure, blue colors refer to negative values while red colors refer to positive values of contours. Clearly, the POD modes are almost even or odd functions in y as it is the case for the symmetric configuration at no incidence ($\alpha = -22.5^\circ$) as reported in the literature (see e.g. [5,8,9]). Here, given that the baseline configuration is asymmetric, this is only approximately

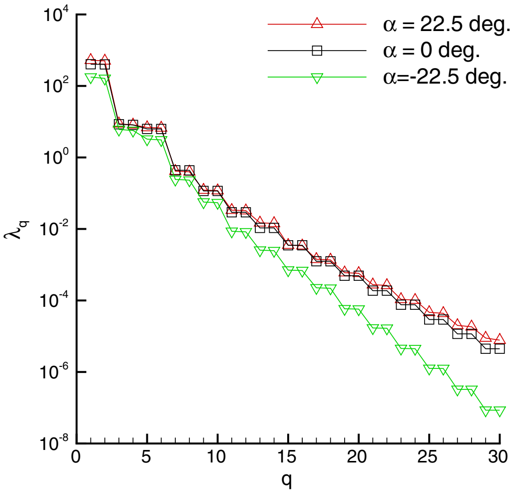

Fig. 13. First half of POD spectra for different incidences.

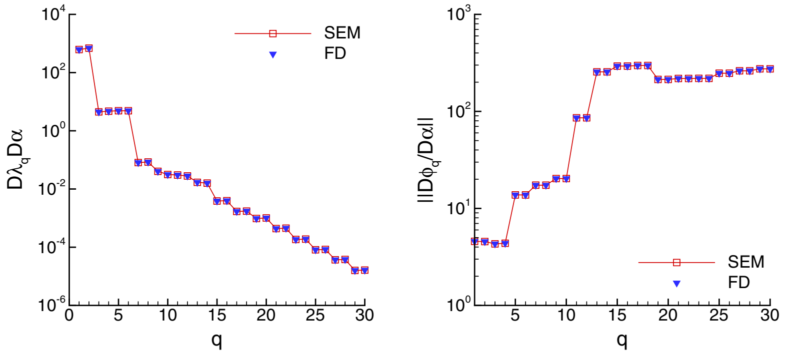

(a) First half of the POD spectrum sensitivity (b) Norm of the first 30 POD mode sensitivities

Fig. 14. Sensitivity of the POD at the baseline state: comparison between FD and SEM approaches.

true. However, the POD modes can be grouped by pairs, as for symmetric configurations, since this property comes from the temporal periodicity of the flows, which here is preserved through any parameter change, and makes the temporal eigenfunctions Fourier modes (see [10] for details). This is also the reason why the eigenvalues decay pairwise in Fig. 13.

A qualitative picture of the structure of the POD mode sensitivities is given in Fig. 16 where contours of the streamwise and normal components of the first four POD mode sensitivities are presented. Clearly, they contain different structures than the original POD modes. To make this point clear, components of the POD modes have been removed from the sensitivities shown in Fig. 16 by orthogonalizing (using a QR decomposition) the set of vectors comprised of the POD modes and their sensitivities. The POD eigenfunctions are not modified by this operation since they already form a set of orthonormal vectors. However, the POD modes and their sensitivities have been made maximally linearly independent by extracting an orthonormal basis from these vectors. The resulting *orthogonalized* sensitivities shown in Fig. 16 are linearly independent of the POD basis components and thus span a different subspace. Note also that their influence is not only significant in the vicinity of the cylinder but also in its wake.

5.4. Reduced-order approximations

This section reports the performance of reduced-order approximations built from the bases described in Section 3.4 for the short term dynamic of flows. To focus on the influence of the basis used in the reduced-order modeling, all ROM simulations are initialized using the DNS data at the considered state and use the appropriate centering (note, however, that in the context of the extrapolated idea, the mean flow can be extrapolated using the sensitivity of the mean flow which is easily calculated from the flow sensitivities at the baseline; and for the expanded approach, the low-dimensional basis can be expanded by the sensitivity of the mean flow to take into account the mean flow modification through parameter changes; the interested reader is referred to [11] for details.) As in Section 4.3, we compare the low-dimensional solutions $\mathbf{u}^r$ to the full-order solution obtained by a DNS at the perturbed state $\mathbf{u}^{DNS}|_\alpha$ by measuring the error in $\mathbf{u}^r$ from (47). We also look at the error in $\mathbf{u}^p$ where the time coefficients are obtained by projection on the DNS data (see Section 4.3). Fig. 17 reports errors for bases of dimension 6 and 12 in $\mathbf{u}^p$ (Fig. 17(a) and (c), respectively) and $\mathbf{u}^r$ (Fig. 17(b) and (d), respectively). As can be seen in Fig. 17(a) and (c), the two sensitivity-based bases provide a better approximation of the data (error in $\mathbf{u}^p$) than the baseline basis. This is true for all parameter perturbations but the best improvements are obtained around the baseline as expected. At the baseline, all bases perform the same since they all contain at least the first q POD modes at this state. The baseline, perturbed and extrapolated bases are all the same and only the expanded basis is different due to the additional POD mode sensitivities. This result shows that the baseline sensitivity modes do not represent a significant part of the energy in the baseline data and that the POD modes alone provide an efficient low-dimensional basis for the baseline flow. However, when one moves away from the baseline state, the baseline POD basis loses its ability to approximate flow solutions so that the baseline approach becomes inaccurate. At these points, the mode sensitivities provide relevant directions to account for perturbations in solutions due to parameter changes. Close to the baseline, this additional information is enough to yield representation errors as low as for the perturbed basis. When one goes further from the baseline in the parameter space this is no longer true. This means that for large parameter perturbations, the first-order POD mode sensitivities cannot account for all changes in the solutions. However, at these states, the extrapolated and expanded bases provide better approximations than the baseline basis.

We now look at errors in low-order approximations of flows obtained from ROM predictions in Fig. 17(b) and (d). As can be seen, similar conclusions hold for the baseline, extrapolated and perturbed approaches. It shows that these ROM capture the dynamics of their basis components fairly well. However, errors in the expanded basis model exhibit a clearly different behavior. The most surprising result occurs at the baseline state. Indeed, the expanded basis contains the first q baseline POD

[redacted]

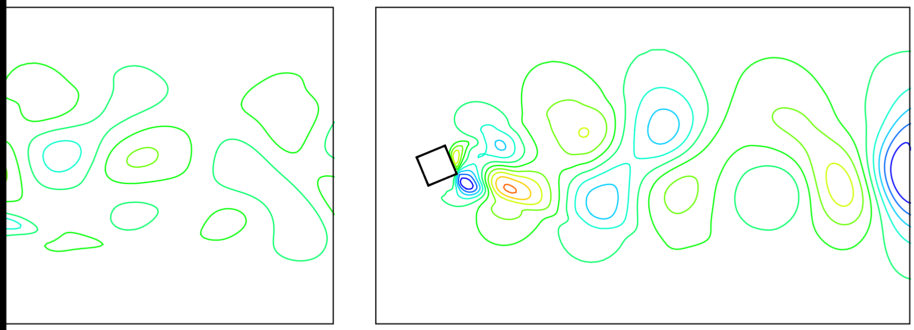

wise component of ϕ_1^α

(b) Normal component of ϕ_1^α

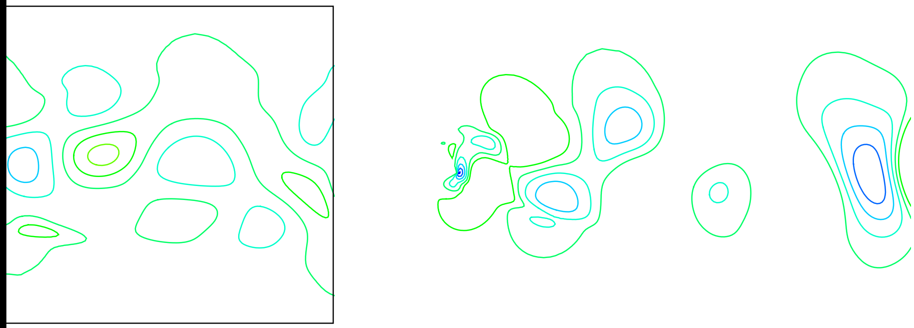

wise component of ϕ_2^α

orthogonal to t [redacted] flow at all times.) However, the dynamical system from the expanded approach incorrectly sends energy from th [redacted] s to the sensitivity components. This leads to unphysical ROM predictions. This incorrect behavior

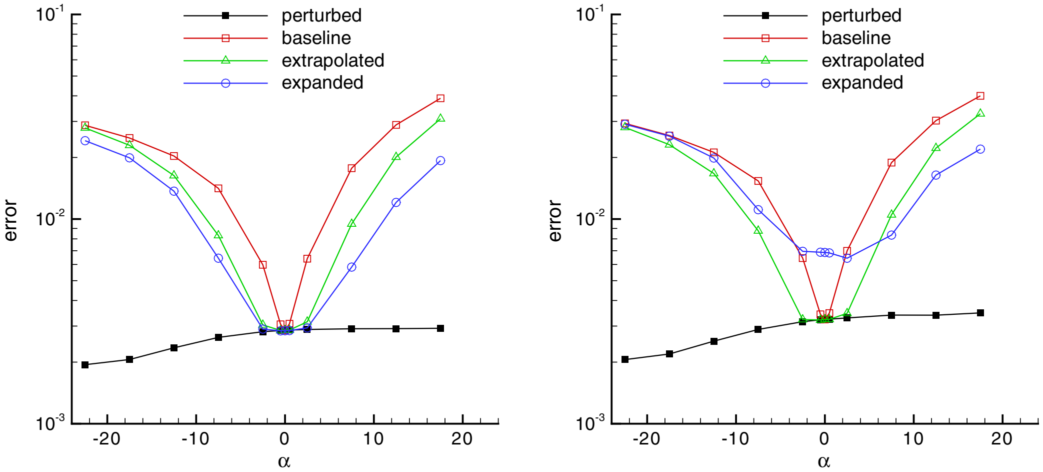

(a) Projection on the perturbed data for $q = 6$

(b) ROM for $q = 6$

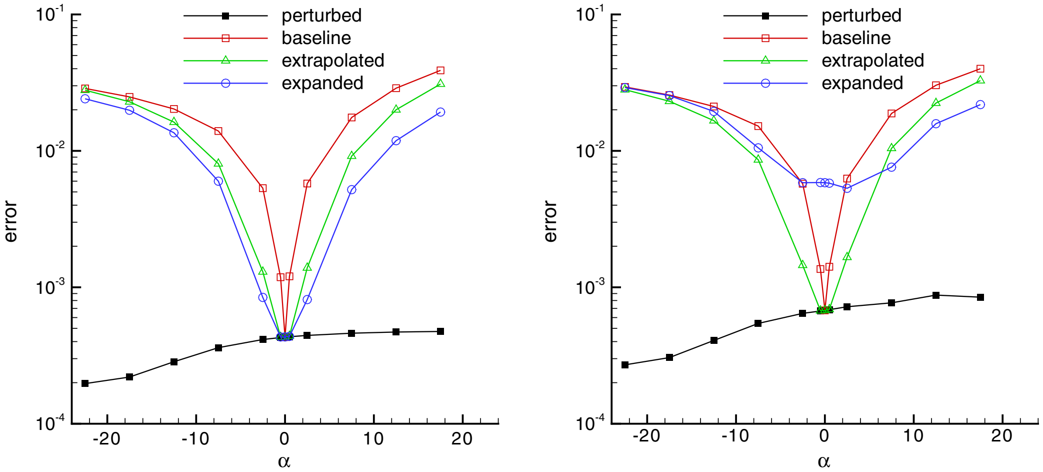

(c) Projection on the perturbed data for $q = 12$

(d) ROM for $q = 12$

Fig. 17. Error in reduced-order solutions as a function of the shape parameter α.

is illustrated in Fig. 18 where the time evolution of modal coefficients a_1 and a_{13} is plotted over a hundred baseline flow periods. As can be seen in (45), a_1 is associated to the first baseline POD mode ϕ_1 of the data decomposition at $\alpha = 0$ while a_{13} is associated to the first baseline sensitivity component ϕ_1^α for $q = 12$. During the initial stage of the simulation, a_{13} is small as expected but grows rapidly with time. This incorrect gain of energy of these basis components will in turn incur inaccurate predictions of the time evolution of a_1. Hence, though the expanded approach provides a better basis in which to approximate solutions over a range of parameter values around the baseline, resulting ROMs fail to predict the short-term dynamics of these flows. This result is a severe drawback for the expanded approach which up to now had provided the best and most robust approach to compute reduced-order approximations of flows over a range of parameter values.

We are currently investigating the reasons of this failure. However, poor behaviors of Galerkin models have already been reported in the literature. Foias et al. [43] investigated the existence of multiple spurious steady states in the Galerkin expansion of the Kuramoto–Sivashinsky equation. For a similar equation, [44] also found spurious states in their POD model that captured 99.99% of the system's energy. They observed that the predicted solution is not the right limit cycle. Noack et al. [7] present a 3-dimensional system of ODE for which a Galerkin reduced-order model is built using an exactly valid decomposition of the full-order solution. They show that the resulting ROM is *structurally unstable* (unlike the full-order system) and has incorrect attractors. A similar result has also been obtained in [45] for another dynamical system for which the Galerkin method gives rise to an unstable attractor. Anttonen et al. [16] report unstable models built using a (blended) POD basis extracted flow snapshots at several different parameter values.

In the reduced-order modeling of vortex shedding, the Galerkin projection introduces spurious limit cycles which may cause the solution to drift to a nonphysical state. However, it is typically observed in the long-time integration of the low-dimensional system where the solution can drift to some erroneous state even if it is initialized with the correct periodic

are linearly altered by modifications in the problem geometry through changes in parameter values. They are the key element in the study to build reduced-order approximations for problems with parameter dependent geometries.

Shape sensitivity analysis of the POD consists in the differentiation of the eigenvalue problem to which the POD functions are solutions. The complete methodology has been presented in details. As expected, it requires the sensitivity of the flow data that is decomposed to yield the POD modes. While it can easily be obtained by finite-differences of two nearby flow datasets, this is a costly approach since it makes the mode sensitivities at least as computationally expensive as the POD modes themselves. To mitigate this issue, the sensitivity equation method (SEM) has been used to generate flow sensitivity data that are then obtained for a fraction of the cost of corresponding flow data (largely because sensitivity equations are always linear as opposed to the Navier–Stokes equations). Note also that, as already reported in the literature, there is a number of additional difficulties and limitations associated with the use of finite-differences in shape sensitivity analysis from which the SEM does not suffer.

The solution to the differentiated eigenvalue problem provides both the sensitivity of the eigenvalues and the POD spatial and temporal modes. This information is valuable because the POD is not only used for model building purposes but also for flow characterization. As an example, for the flows over square cylinders at incidence, the sensitivity of the eigenvalues with respect to the angular orientation of the cylinder are all positive indicating that an increase in this parameter will lead to an increase of the total kinetic energy of the flow.

In the context of reduced-order modeling, the POD mode sensitivities have been used in the basis selection step to enlarge the set of solutions than can be accurately represented in the parameter space. To this end, we have examined two different approaches. This first one extrapolates the POD modes in the parameter space to the corresponding state to be modeled. It relies on the assumption that these eigenfunctions have a linear dependency on the parameters that can only be validated locally. The second one expands the low-dimensional POD basis by adding the sensitivity of the original components. The underlying idea behind this approach is that the POD mode sensitivities span a different subspace than the one generated by the POD eigenfunctions and *point* in relevant directions when considering parameter changes. This property has been demonstrated in previous studies by the authors [11].

The improvements yielded by these new bases in terms of reduced-order flow approximations have been tested for the one-dimensional Burgers' equation and the two-dimensional Navier–Stokes equations. In both cases, the sensitivity-based bases provide a more reliable and robust alternative to using only the baseline POD modes to accurately approximate solutions for a range of parameter values and thus a set of different geometries. Results are more impressive for the simpler case of the one-dimensional Burgers' equation. Indeed, even for large parameter changes, the expanded basis built at the baseline can potentially be as adequate as the bases obtained by decompositions of flow data at perturbed states. All in all, the expanded approach usually yields a better and more robust alternative than the extrapolated approach but essentially doubles the basis dimension.

For the Burger' equation problem, all ROM built using the sensitivity-based bases have successfully predicted the correct dynamics of all modal components in the low-dimensional approximation at hand. Hence, the improvements observed previously are inherited by the ROM solutions and thus more robust reduced-order models are obtained. However, a serious limitation has been uncovered when considering two-dimensional flows over cylinders at incidence. For this case, the expanded basis has led to ROM having incorrect behaviors (note that the extrapolated approach is not subjected to this problem). The most striking example is observed at the baseline where energy is transferred from the POD modes to their sensitivities though the latter components should not be activated at all. Although this is in contrast with previous studies on several cases, it clearly stresses that even when having a low-dimensional basis accounting for a huge fraction of the solution energy (the expanded basis with $q = 12$ captures more than 99.99% of the baseline flow energy), there is no guarantee that the corresponding reduced-order dynamical system is a good approximation of the full-order system. In particular, it may have different attractors so that the ROM solutions have incorrect limit cycles. Here, the expanded ROM cannot correctly approximate the short-term dynamics of the full-order solution. Future research will aim at understanding this failure and try to provide a remedy to it. Similar problems in reduced-order modeling has already be reported in the literature and a number of approaches have been proposed to improve or correct POD model behaviors. As an example, the procedures proposed by Couplet et al. [9] which rely on minimization problems to produce improved ROM by calibrating their polynomial coefficients may be used. Alternatively, a shooting method [48] may help to prevent the reduced-order system to drift to an unphysical limit cycle.

Acknowledgments

This research was supported in part by the Air Force Office of Scientific Research (under contract FA9550-08-1-0136), the National Science Foundation (under contract DMS-0513542), the National Science and Engineering Council of Canada, and the Canadian Research Chair Program.

Imran Akhtar would like to thank the Government of Pakistan for financial support during part of his graduate studies.

References

[1] M. Loève, Probability Theory, Van Nostrand, New York, 1955.
[2] P. Holmes, J. Lumley, G. Berkooz, Turbulence, Coherent Structures, Dynamical Systems and Symmetry, Cambridge University, 1996.

[3] L. Sirovich, Turbulence and the dynamics of coherent structures, Part I: coherent structures, Quart. Appl. Math. 45 (3) (1987) 561–571.
[4] N. Aubry, On the hidden beauty of the proper orthogonal decomposition, Theor. Comput. Fluid Dyn. 2 (1991) 339–352.
[5] E. Deane, I. Kevrekidis, G. Karniadakis, S. Orszag, Low-dimensional models for complex geometry flows : application to grooved channels and circular cylinders, Phys. Fluids A 3 (10) (1991) 2337–2354.
[6] B. Galletti, C. Bruneau, L. Zannetti, A. Iollo, Low-order modelling of laminar flow regimes past a confined square cylinder, J. Fluid Mech. 503 (2004) 161–170.
[7] B. Noack, K. Afanasiev, M. Morzyński, G. Tadmor, F. Thiele, A hierarchy of low-dimensional models for the transient and post-transient cylinder wake, J. Fluid Mech. 497 (2003) 335–363.
[8] S. Sirisup, G. Karniadakis, A spectral viscosity method for correcting the long-term behavior of POD models, J. Comput. Phys. 194 (2004) 92–116.
[9] M. Couplet, C. Basdevant, P. Sagaut, Calibrated reduced-order POD-Galerkin system for fluid flow modeling, J. Comput. Phys. 207 (1) (2005) 192–220.
[10] A. Hay, J. Borggaard, D. Pelletier, On the use of sensitivity analysis to improve reduced-order models, in: Fourth AIAA Flow Control Conference, Seattle, Washington, 2008, AIAA-2008-4192.
[11] A. Hay, J. Borggaard, D. Pelletier, Improved low-order modelling from sensitivity analysis of the proper orthogonal decomposition, J. Fluid Mech. 629 (2009) 41–72.
[12] J. Borggaard, J. Burns, A PDE sensitivity equation method for optimal aerodynamic design, J. Comput. Phys. 136 (2) (1997) 367–384.
[13] D. Pelletier, A. Hay, S. Etienne, J. Borggaard, The sensitivity equation method in fluid mechanics, Eur. J. Comput. Mech. 17 (1–2) (2008) 31–61.
[14] F. Ilinca, D. Pelletier, A. Hay, First- and second-order sensitivity equation methods for value and shape parameters, Int. J. Numer. Meth. Fluids 57 (9) (2008) 1349–1370.
[15] J. Borggaard, A. Hay, D. Pelletier, Interval-based reduced-order models for unsteady fluid flow, Int. J. Numer. Anal. Model. 4 (3–4) (2007) 353–367.
[16] J.S.R. Anttonen, P.I. King, P.S. Beran, POD-based reduced-order models with deforming grids, Math. Comput. Model. 38 (2003) 41–62.
[17] X. Ma, G. Karniadakis, A low-dimensional model for simulating three-dimensional cylinder flow, J. Fluid Mech. 458 (2002) 181–190.
[18] T. Lieu, C. Farhat, M. Lesoinne, Reduced-order fluid/structure modeling of a complete aircraft configuration, Comput. Meth. Appl. Mech. Eng. 195 (2006) 5730–5742.
[19] D. Amsallem, C. Farhat, Interpolation method for adapting reduced-order models and application to aeroelasticity, AIAA J. 46 (7) (2003) 1803–1813.
[20] A. Hay, D. Pelletier, R.D. Caro, Verified predictions of shape sensitivities in wall-bounded turbulent flows by an adaptive finite-element method, J. Comput. Phys. 228 (12) (2009) 4510–4531.
[21] E.J. Nielsen, W.K. Anderson, Aerodynamic design optimization on unstructured meshes using the Navier–Stokes equations, AIAA J. 37 (11) (1999) 1411–1419.
[22] M. Nemec, D.W. Zingg, T.H. Pulliam, Multi-point and multi-objective aerodynamic shape optimization, AIAA J. 42 (6) (2004) 1057–1065.
[23] F. Ilinca, D. Pelletier, A continuous shape sensitivity equation method for unsteady laminar flows, Int. J. Comput. Fluid Dyn. 21 (7–8) (2007) 255–266.
[24] J.R.R.A. Martins, P. Stradza, J.J. Alonso, The complex-step derivative approximation, ACM Transactions on Mathematical Software – TOMS 29 (3) (2003) 245–262.
[25] W.K. Anderson, J.C. Newman, D.L. Whitfield, E.J. Nielsen, Sensitivity analysis of Navier–Stokes equations on unstructured meshes using complex variables, AIAA J. 39 (1) (2001) 56–63.
[26] S.-Y. Lu, P. Sagaut, Direct sensitivity analysis for smooth unsteady compressible flows using complex differentiation, Int. J. Numer. Meth. Fluids 53 (12) (2007) 1863–1886.
[27] A. Griewank, Some bounds on the complexity of gradients, in: Pardalos, P. (Ed.), Jacobians and Hessians, Complexity in Nonlinear Optimization, World Scientific Publishers, River Edge, NJ, 1993.
[28] E. Laporte, P.L. Tallec, Numerical methods in sensitivity analysis and shape optimization, Birkhäuser, Boston, 2003.
[29] B. Mohammadi, O. Pironneau, Shape optimization in fluid mechanics, Ann. Rev. Fluid Mech. 36 (2004) 255–297.
[30] J. Borggaard, A. Verma, On efficient solutions to the continuous sensitivity equation using automatic differentiation, SIAM J. Sci. Comput. 22 (1) (2000) 39–62.
[31] J. Batina, Unsteady Euler airfoil solutions using unstructured dynamic meshes, in: AIAA 27th Aerospace Sciences Meeting, AIAA Paper 89-0115, Reno, Nevada, 1989.
[32] C. Farhat, C. Degand, B. Koobus, M. Lesoinne, Torsional springs for two-dimensional dynamic unstructured fluid meshes, Comput. Meth. Appl. Mech. Eng. 163 (1) (1998) 231–245.
[33] P. Sackinger, P. Schunk, R. Rao, A Newton–Raphson pseudo-solid domain mapping technique for free and moving boundary problems: a finite-element implementation, J. Comput. Phys. 125 (1996) 83–103.
[34] S. Etienne, D. Pelletier, A general approach to sensitivity analysis of fluid structure interactions, J. Fluids Struct. 21 (2005) 169–186.
[35] A. Sohankar, C. Norberg, L. Davidson, Numerical simulation of unsteady low-Reynolds number flow around rectangular cylinders at incidence, J. Wind Eng. Ind. Aerodyn. 69–71 (1997) 189–201.
[36] A. Sohankar, C. Norberg, L. Davidson, Low-Reynolds number flow around a square cylinder at incidence : study of blockage, onset of vortex shedding and outlet boundary condition, Int. J. Num. Meth. Fluids 26 (1) (1998) 39–56.
[37] A. Sohankar, C. Norberg, L. Davidson, Simulation of three-dimensional flow around a square cylinder at moderate Reynolds numbers, Phys. Fluids 11 (2) (1999) 189–201.
[38] A. Hay, A. Leroyer, M. Visonneau, H-adaptive Navier–Stokes simulations of free-surface flows around moving bodies, J. Mar. Sci. Technol. 11 (1) (2006) 1–18.
[39] R. Fox, M. Kapoor, Rates of change of eigenvalues and eigenvectors, AIAA J. 6 (12) (1968) 2426–2429.
[40] D. Murthy, R. Haftka, Derivatives of eigenvalues and eigenvectors of a general complex matrix, Int. J. Numer. Meth. Eng. 26 (1988) 293–311.
[41] P. Lancaster, On eigenvalues of matrices dependent on a parameter, Numer. Math. 6 (1964) 377–387.
[42] A. Seyranian, E. Lund, N. Olhoff, Multiple eigenvalues in structural optimization problems, Struct. Optim. 8 (1994) 207–227.
[43] C. Foias, M.S. Jolly, I.G. Kevrekidis, E.S. Titi, Dissipativity of the numerical schemes, Nonlinearity 4 (1991) 591–613.
[44] N. Aubry, W.Y. Lian, E.S. Titi, Preserving symmetries in the proper orthogonal decomposition, SIAM J. Sci. Comput. 14 (2) (1993) 483–505.
[45] D. Rempfer, On low-dimensional Galerkin models for fluid flow, Theor. Comput. Fluid Dyn. 14 (2) (2000) 75–88.
[46] E. Tadmor, Convergence of spectral methods for nonlinear conservation laws, SIAM J. Numer. Anal. 26 (1) (1989) 30.
[47] I. Akhtar, A.H. Nayfeh, C.J. Ribbens, On the stability and extension of reduced-order Galerkin models in incompressible flows: a numerical study of vortex shedding, Theor. Comput. Fluid Dyn. 23 (3) (2009) 213–237.
[48] A.H. Nayfeh, B. Balachandran, Applied Nonlinear Dynamics: Analytical, Computational, and Experimental Methods, Wiley, New York, NY, 1995.